SACLANTCEN Report SR - 83

SACLANTCEN Report SR - **83**

SACLANT ASW RESEARCH CENTRE REPORT

REVIEW OF NUMERICAL MODELS IN UNDERWATER ACOUSTICS, INCLUDING RECENTLY DEVELOPED FAST-FIELD PROGRAM

by
Finn B. JENSEN
Henrik SCHMIDT

15 DECEMBER 1984

NORTH ATLANTIC TREATY ORGANIZATION

SACLANTCEN
LA SPEZIA, ITALY

Published by

STI

SACLANTCEN

SACLANTCEN REPORT SR-83

NORTH ATLANTIC TREATY ORGANIZATION

SACLANT ASW Research Centre
Viale San Bartolomeo 400,
I-19026 San Bartolomeo (SP), Italy.

tel: national 0187 540111
international + 39 187 540111

telex: 271148 SACENT I

REVIEW OF NUMERICAL MODELS IN UNDERWATER ACOUSTICS, INCLUDING RECENTLY DEVELOPED FAST-FIELD PROGRAM

by

Finn B. Jensen
Henrik Schmidt

(SACLANTCEN papers presented at the NATO Advanced Research Workshop on Hybrid Formulation of Wave Propagation and Scattering, Rome, 30 August - 3 September 1983)

15 December 1984

This report has been prepared as part of Project 19.

APPROVED FOR DISTRIBUTION

Ralph R. Goodman

RALPH R. GOODMAN
Director

TABLE OF CONTENTS

ABSTRACT

Two papers given by SACLANTCEN personnel at the NATO Advanced Research Workshop on Hybrid Formulation of Wave Propagation and Scattering in Castel Gandolfo, Rome, Italy on 30 August to 3 September 1983 are published as a review of SACLANTCEN's recent programme in underwater-acoustic modelling. The first briefly reviews the physics of sound propagation in the ocean. In it the mathematical foundations of the most widely used acoustic models (ray, mode, fast field, parabolic equation) are presented and the areas of applicability of the various models are indicated. A few numerical examples are included to show the consistency among the different computer models in overlapping regimes of validity. A series of computational examples is given to demonstrate the applicability of these models to a wide range of general wave-propagation problems. The second paper presents a new numerical model, of the fast field type, where the depth-separated wave equation is solved by a numerical technique very similar to that used in finite-element programs. The speed improvement over existing models of the same type is considerable, especially in cases with many sources and receivers. The model has been used for studying both seismic pulse propagation in shallow water and reflection of pulsed ultrasonic beams from a fluid/solid interface.

PREFACE

This report contains two SACLANTCEN contributions to a NATO Advanced Research Workshop on Hybrid Formulation of Wave Propagation and Scattering, held in Castel Gandolfo, Rome, Italy, on 30 August to 3 September 1983. The Workshop was directed by Professor L.B. Felsen, Polytechnic Institute of New York, with the scope of bringing together researchers in different fields of wave propagation (electromagnetics, optics, seismics, underwater acoustics) to exchange ideas and approaches to solving complex wave-propagation problems.

SACLANTCEN was invited to present two papers: a review of numerical models in underwater acoustics (F.B. Jensen), and a recently developed solution technique of the fast-field type (H. Schmidt). These two papers are here published as a single report, since it is felt that together they give a good representation of the successful research programme of SACLANTCEN's Environmental Modelling Group over the past years.

The full proceedings of the Workshop, containing 24 contributions, is available in <1>.

<1> FELSEN, L.B. ed. Hybrid Formulation of Wave Propagation and Scattering. Dordrecht, Netherlands, Martinus Nijhoff, 1984.

NUMERICAL MODELS IN UNDERWATER ACOUSTICS

Finn B. Jensen

SACLANT ASW Research Centre
Viale San Bartolomeo 400
19026 La Spezia, Italy

ABSTRACT

The physics of sound propagation in the ocean is briefly reviewed. The mathematical foundation of the most widely used acoustic models (ray, mode, fast field, parabolic equation) is presented and the areas of applicability of the various models are indicated. A few numerical examples are included to show the consistency among the different computer models in overlapping regimes of validity. Finally, we show a series of computational examples that demonstrate the applicability of these models to a wide range of general wave-propagation problems.

INTRODUCTION

The modern era of underwater acoustics essentially dates back to the beginning of World War II, where considerable effort went into improving submarine detection by acoustic means. This effort has continued, promoted by naval interests in developing still better and more reliable sonar systems. To achieve optimum sonar design one needs to know how sound propagates in the ocean as a function of frequency for different source/receiver configurations and for different environmental conditions.

By now the theory of acoustic propagation is well developed, providing both a good general understanding and a detailed description of how sound travels in the ocean. The theoretical basis is the acoustic wave equation, which has to be solved with realistic boundary conditions at the sea surface and at the sea floor. This problem is generally too complex for applying analy-

tical solutions, and hence we must resort to numerical methods. Several solution techniques (ray, mode, FFP, PE) have been introduced over the years, with the acoustic models increasing in complexity as computers became faster and more powerful. Ray theory was the only practical technique for solving propagation problems until the beginning of the 1970s. Then advances in computer technology made it possible to consider solving more complex equations, and, consequently, new techniques (normal mode, fast field, parabolic equation) came into extensive use during the last decade.

In this paper we outline the basics of sound propagation in the ocean, including important propagation and loss mechanisms, and a simplified environmental description for use in numerical models. We then proceed to outline the mathematical foundation of the most widely used numerical models, and we demonstrate the consistency and inter-relationship between the various models through a few numerical examples for deep and shallow water environments. We then indicate the areas of applicability of the various acoustic models taking into account both limitations in the underlying theory and the numerical efficiency of the actual computer codes. A demonstration of the wide range of applicability of these ocean-acoustic models is provided by a series of computational examples, where the models have been applied to some general wave propagation problems, including beam reflection at fluid/solid interfaces, propagation from ducts into free-space, up- and down-slope propagation involving mode coupling and mode cutoff.

2 SOUND PROPAGATION IN THE OCEAN

The goal of ocean acoustic modelling is to estimate the spatial properties of the sound pressure field as a function of source frequency. To clarify the complexity of the modelling problem, let us briefly review the environmental acoustics of the ocean. Figure 1 is a schematic of some important sound propagation paths; two possible sound-source locations are on the left and sound is propagating from left to right. Two dashed lines at 0 and 80 km range indicate two of the innumerable ways in which sound speed in the water can vary with depth from place to place (or from time to time). Lines A, B, C, and D represent four possible sound-propagation paths whose shapes are determined by the location of the source and the sound-speed structure over the extent of the propagation.

Path A from the shallow source is "surface-duct" propagation, because the sound-speed profile is such that the sound is trapped near the surface of the ocean. Paths B, C, and D are from the deeper source. Ray B, leaving the source at a small angle from

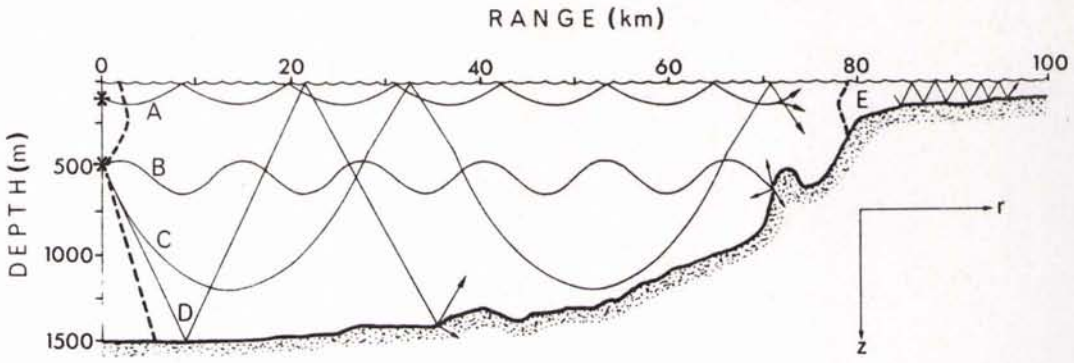

Fig. 1 Schematic of sound propagation in the ocean

the horizontal, tends to propagate in the "deep sound channel" without interacting with the boundaries (surface and bottom) of the ocean. At slightly steeper angles (path C) we have "convergence zone" propagation, which is a spatially periodic phenomenon of zones of high intensity near the surface. Here sound interacts with the ocean surface but not with the bottom. Path D is the "bottom-bounce path", which has a shorter cycle period than the convergence zone path. The right-hand side of Fig. 1 depicts propagation on the continental shelf (shallow water) where a complicated bottom structure combined with variable sound-speed profiles result in rather complicated propagation conditions not always suited for a ray representation.

Our ability to model acoustic propagation effectively in the ocean is determined by the accuracy with which acoustic loss mechanisms in the ocean environment are handled. Aside from geometrical spreading loss (spherical, cylindrical, etc.) the main loss mechanisms are volume absorption, bottom-reflection loss, surface and bottom scattering loss.

Volume absorption in sea water, caused by viscosity and chemical relaxation, increases with increasing frequency. This loss mechanism is the dominant attenuation factor associated with path B in Fig. 1, since this path does not interact with the boundaries. Because there is very little volume absorption at low frequencies, deep-sound-channel propagation has been observed to distances of many thousands of kilometres.

When sound interacts with the sea floor, the nature of the bottom becomes important. Figure 2 depicts simple bottom-loss curves, with zero dB loss indicating perfect reflection. For an ideal bottom without volume absorption (non-lossy) we still get severe reflection loss above a certain critical angle θ_c due to transmission into the bottom. For a real bottom with volume

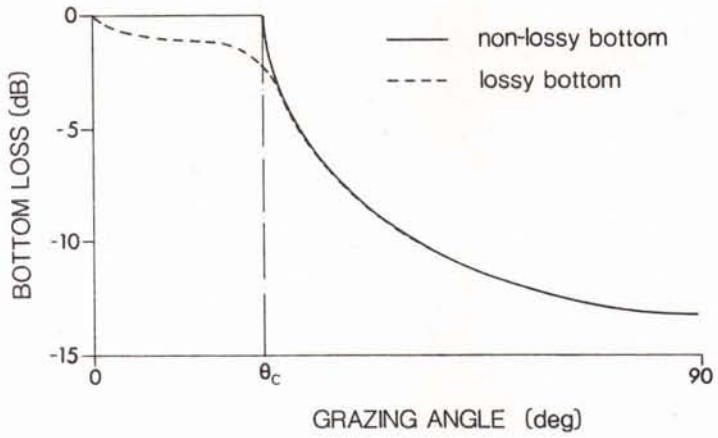

Fig. 2 Bottom loss versus grazing angle

absorption (lossy) we never get perfect reflection, even though the curves look similar. Path D in Fig. 1, the bottom-bounce path, often corresponds to angles near or above the critical angle; therefore after a few bounces it is highly attenuated. On the other hand, for shallower angles, many more bounces are possible; hence in shallow water (path E) most of the energy that propagates is close to the horizontal. In reality, much of the ocean bottom is layered and also supports shear waves; in this case bottom loss becomes a complicated function of frequency and grazing angle. The overall effect of bottom loss on sound propagation in the water column is an increasing loss with decreasing frequency.

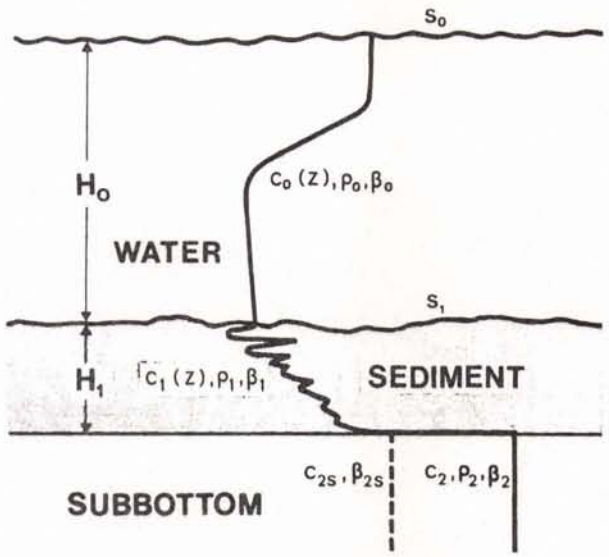

Fig. 3 Environmental input to ocean acoustic models

A rough sea surface or sea floor causes scattering of the incident sound. The result is a decay of the mean acoustic field in the water column as a function of range (scattering loss), with the scattered energy being lost to the ocean bottom through steep-angle propagation. The scattering loss increases with increasing frequency, and the propagation paths mainly affected are paths A and C (surface scattering loss) and paths D and E (surface and bottom scattering loss).

A consistent mathematical model of sound propagation in the ocean must contain the physics that governs the above-mentioned propagation and loss mechanisms. A summary of the environmental inputs needed for a realistic description of the ocean waveguide is given in Fig. 3. In this simplified model the ocean consists of a water column of depth H_0 limited by a rough sea surface and a rough sea floor. The sound speed c_0 in the water column may vary arbitrarily with depth, while density ρ_0 and attenuation β_0 are considered constant. Even though real ocean bottoms exhibit a complicated layering, we have found that a simple two-layered geoacoustic model generally provides the necessary degrees of freedom to accurately include bottom effects in numerical models for many ocean areas. Hence the bottom may consist of just a sediment layer of thickness H_1 and a semi-infinite subbottom. The model should allow for sound speed, density, and attenuation to vary arbitrarily with depth in the sediment layer, while the subbottom can be considered homogeneous. It is desirable that the model can handle shear-wave propagation in both bottom layers. Finally, in real ocean environments the parameters given in Fig. 3 may all vary with range.

3 MATHEMATICAL FOUNDATION OF OCEAN ACOUSTIC MODELS

We briefly present the mathematical foundations of the four models discussed in this paper. A more detailed description can be found in references <1-10>.

The starting point for all the models is the wave equation for a harmonic point source with time dependence $\exp(-i\omega t)$,

$$\nabla^2\phi(x,y,z) + \left[\frac{\omega}{c(x,y,z)}\right]^2 \phi(x,y,z) = -\delta(x-x_0)\delta(y-y_0)\delta(z-z_0) \tag{1}$$

$$\psi = \phi\exp(-i\omega t) \tag{2}$$

At any point (x,y,z) in the medium, the velocity potential ϕ satisfies Eq. (1) where $c(x,y,z)$ is the sound speed of the medium

and δ is the Dirac delta function. The source is at the coordinate (x_o, y_o, z_o) where z is the depth coordinate, which is taken to be positive in the downward direction from the ocean surface.

For the boundary condition at the ocean surface we take the density of air to be negligible compared with that of water; hence, the pressure must vanish at the ocean surface ("pressure-release surface"). At a boundary between two media such as the ocean and the ocean bottom, the balancing of forces at the interface require that physical quantities such as particle velocity and pressure be continuous across the boundary:

$$v_i = -\frac{\partial \phi}{\partial x_i} \; ; \; x_i = x, y, \text{ or } z \tag{3}$$

$$p = -i\omega\rho\phi \tag{4}$$

If the ocean bottom is treated as an elastic medium that can support shear motions, there is the additional boundary condition that tangential stress must be continuous. Since the water column cannot support shear waves, this requires that the tangential stress in the ocean bottom vanishes at the interface.

Four widely used solution techniques for Eq. (1) are schematically represented in Fig. 4. The derivation of the classical ray solution can be found in most text books on acoustics, as can the details of the well-established normal-mode solution. The fast-field technique is not yet in standard text books, but it is a powerful tool for solving propagation problems in stratified environments. The parabolic equation technique is a recent advent in acoustic modelling. This method is particularly suited for propagation in range-dependent environments.

We briefly describe the derivation of the above four solution techniques, starting with range-independent wave theory.

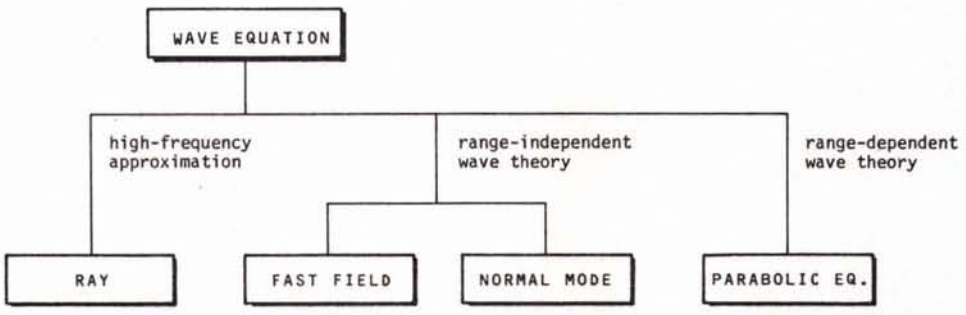

Fig. 4 Four techniques for solving the wave equation

3.1 Fast field solution

Here we are solving the wave equation for the case where the sound-speed profile is only a function of depth and the bottom is flat; this type of environment is often referred to as the horizontally stratified ocean. From Eq. (1) we therefore have that $c(x,y,z)$ is simply $c(z)$. Because the environment is independent of "r", the horizontal coordinates (x,y), one possible method of solving Eq. (1) is to Fourier decompose the acoustic field into an infinite set of horizontal waves:

$$\phi(x,y,z) = \frac{1}{2\pi} \int d^2\vec{\eta}\, u(\vec{\eta},z)\, e^{i\vec{\eta}\cdot\vec{r}} . \tag{5}$$

Substituting Eq. (5) into Eq. (1) we obtain the equation for $\phi(\eta_x,\eta_y;z)$,

$$\frac{\partial^2 u(\eta_x,\eta_y;z)}{dz^2} + [k^2(z) - \eta^2]u(\eta_x,\eta_y;z) = -\frac{1}{2\pi}\delta(z-z_o), \tag{6}$$

where $k(z) = \omega/c(z)$ and $\eta^2 = \eta_x^2 + \eta_y^2$, is the horizontal wavenumber of the individual plane waves.

Using polar coordinates we can rewrite Eq. (5) as

$$\phi(r,z) = \frac{1}{2\pi} \int_0^{2\pi} d\theta \int_0^{\infty} \eta\, d\eta\, u(\eta,z) e^{i\eta r\cos\theta}. \tag{7}$$

We now integrate over the azimuthal angle to obtain

$$\phi(r,z) = \int_0^{\infty} \eta\, d\eta\, u(\eta,z) J_o(\eta r), \tag{8}$$

where J_o is the zeroth order Bessel function. Using the relationship that

$$J_o(\eta r) = 1/2\, [H_o^{(1)}(\eta r) + H_o^{(2)}(\eta r)],$$

where the H's are Hankel functions and noting from Eq. (6) that $u(\eta,z)$ is even in η, we can rewrite Eq. (8) as

$$\phi(r,z) = 1/2 \int_{-\infty}^{\infty} \eta\, d\eta\, u(\eta,z)\, H_o^{(1)}(\eta r), \tag{9}$$

where now the integration over η is from $-\infty$ to ∞. For ranges

greater than a few wavelengths from the source, the asymptotic form of the Hankel function can be used:

$$H_o^{(1)}(\eta r) \sim (2/\pi\eta r)^{1/2} \exp[i(\eta r - \pi/4)]$$

and, hence, Eq. (9) can be expressed as

$$\phi(r,z) = \frac{e^{-i\pi/4}}{\sqrt{2\pi}} \cdot \frac{1}{\sqrt{r}} \int_{-\infty}^{\infty} d\eta \sqrt{\eta} u(\eta,z) e^{i\eta r}, \qquad (10)$$

where the factor $1/\sqrt{r}$ indicates cylindrical spreading.

Equation (10) can be numerically integrated to obtain the acoustic field at the range r and depth z. In order to do this we must solve Eq. (6) for many η's to have a sufficient set of u's as a function of η so that the integration over η in Eq. (10) can be performed. Given that u has been obtained numerically as a function of η, the integration can be done using an FFT algorithm. This total procedure is called the Fast Field Program (FFP) <11-13>, although most of the numerical effort goes into solving Eq. (6) for the many η's. For computation we discretize Eq. (10) by letting

$$\eta_m = \eta_o + m\Delta\eta; \; r_n = r_o + n\Delta r; \; (m,n) = 0,1,2\ldots,N-1, \qquad (11)$$

with the additional relation

$$\Delta r \Delta\eta = \frac{2\pi}{N} \qquad (12)$$

and N is an integral power of two. Note that the discretization relations of Eq. (11) restricts the solution to outgoing waves. Substituting Eq. (11) into Eq. (10) we obtain

$$\phi(r_n,z) = \Delta\eta \frac{e^{-i\pi/4}}{\sqrt{2\pi r}} e^{i\eta_o r_n} \sum_{M=0}^{N-1} X_m e^{i2\pi mn/N}, \qquad (13)$$

and hence the input to the FFT is

$$X_m = \sqrt{\eta_m}\, u(\eta_m,z) e^{imr_o\Delta\eta}. \qquad (14)$$

Equations (13) and (14) specify the numerical procedure to be employed in solving the wave equation using the FFP approach after Eq. (6) has been solved numerically for the complete set of u's as a function of η. As mentioned above, the main effort in the FFP approach is the numerical integration of Eq. (6) and not the final implementation of Eqs. (13) and (14), which is a simple FFT com-

putation. Numerical procedures for integrating Eq. (6) are given in references <11-13>.

The first implementation of the FFP approach was done by DiNapoli <11> around 1970. His method is for a stratified fluid environment, and the numerical procedure is quite fast, since it uses recurrence relations of hypergeometric functions to solve Eq. (6) for all the wavenumbers (η's) rather than solve the equation for one η at the time. A more general solution technique was devised by Kutschale <12> for an arbitrary stratification of solid layers. This technique employs the Thomson-Haskell matrix method, and Eq. (6) is here solved separately for each wavenumber. This solution technique is computationally quite slow and there is no efficient way of doing calculations simultaneously for many sources and receivers. The most recent FFP technique was developed by Schmidt <13>. Again the solution is for an arbitrary stratification of homogeneous solid layers. Displacements and stresses are expressed in terms of three scalar potentials for each layer, as described in <14>. Boundary conditions are then matched at each interface yielding a linear system of equations in the Hankel transforms of the potentials. Equation (6) is again solved at discrete horizontal wavenumbers; with the coefficient matrices being of band form, the equations are solved very efficiently by gaussian elimination. This solution technique is considerably faster than the Kutschale technique, and it furthermore allows for an efficient evaluation of the acoustic field for many sources and receivers at a time. This, in turn, means that the model can be applied to a variety of new problems, including beam reflection problems as shown in Sect. 5.1.

The main advantage of the FFP is that it provides the full solution to sound propagation in a multilayered solid medium, and hence consitutes a benchmark against which other approximate solutions can be checked. Its main disadvantage is that the procedure is not easily automated.

3.2 Normal-mode solution

The alternative to a direct numerical integration of Eq. (6) is to expand u into a complete set of normal modes:

$$u(\eta_x,\eta_y;z) = \Sigma\, a_n(\eta_x,\eta_y)u_n(z), \tag{15}$$

where the u_n's are the solutions to the eigenvalue equation

$$\frac{d^2u_n(z)}{dz^2} + [k^2(z) - k_n^2]u_n(z) = 0 \tag{16}$$

that satisfies the above-mentioned boundary conditions. In addi-

tion, we require the $u_n(z)$ be bounded as $z \to \infty$. The normal modes $u_n(z)$ form a complete orthogonal set that satisfies the relation

$$\int_0^\infty \rho(z)u_n(z)u_m(z)dz = \delta_{nm}, \tag{17}$$

where the density $\rho(z)$ takes its appropriate value in each layer and δ_{nm} is the Kronecker-delta symbol. The spectrum of eigenvalues consists of a discrete part and a continuous part, the discrete eigenvalues occurring in the interval

$$\omega/c_2 < k_n < \max[\omega/c(z)], \tag{18}$$

where c_2 is the highest speed of the system. In the present treatment we consider only the discrete eigenvalues, since, in general, the continuous spectrum makes a negligible contribution beyond the nearfield of the source (and requires an FFP-type calculation in any event).

We now substitute Eq. (15) into Eq. (6), multiply the resulting equation by $\rho(z)u_m(z)$, and integrate over z from 0 to ∞, giving:

$$a_n = \frac{1}{2\pi} \frac{\rho(z_o)u_n(z_o)}{\eta^2-k_n^2} \tag{19}$$

Substituting Eqs. (15) and (19) back into Eq. (5) we obtain an integral representation of the velocity potential,

$$\phi(x,y,z) = \frac{\rho(z_o)}{(2\pi)^2} \int_{-\infty}^{\infty} d\eta_x \int_{-\infty}^{\infty} d\eta_y \sum_n \frac{u_n(z_o)u_n(z)}{\eta^2-k_n^2}$$

$$\times \exp[i(\eta_x x + \eta_y y)]. \tag{20}$$

We evaluate the above integral by choosing a path about the poles so as to lead to an outgoing wave from the source point r = 0. Each integral in Eq. (20) is proportional to the two-dimensional plane-wave representation of the zero-order Hankel function of the first kind <15>, and therefore $\phi(x,y,z)$ can be expressed as:

$$\phi(r,z) = \frac{i}{4} \rho(z_o) \sum_n u_n(z_o)u_n(z)H_o^{(1)}(k_n r). \tag{21}$$

The asymptotic form of the Hankel function can then be used to obtain

$$\phi(r,z) = \frac{i\rho(z_o)}{(8\pi r)^{1/2}} e^{-i\pi/4} \sum_n \frac{u_n(z_o)u_n(z)}{k_n^{1/2}} e^{ik_n r}. \qquad (22)$$

In addition to the decay of the field due to cylindrical spreading, other loss mechanisms such as volume attenuation in the water column and bottom are included in Eq. (22) because the eigenvalues, k_n, have positive imaginary parts <16>, thereby resulting in an exponential attenuation of each normal-mode term. Equation (22) gives us the important result that the field at a depth z is proportional to a sum of the products of normal modes evaluated at the source and the receiver depth. The normal modes are the "natural vibrations" of the system and if a point source is located at the null of a particular normal mode, that mode will not be excited. Similarly, if a point receiver is placed at the null of a particular mode, that mode contribution to the total field will not be sensed.

In analogy to the FFP procedure, the main numerical effort for the normal-mode procedure is the solution of the eigenvalue problem defined by Eq. (16) and the boundary conditions. There are many techniques to solve this equation <17-18> but they are mainly applicable to low-frequency or shallow-water propagation, where there is only a small number of modes <19>. However, there are also techniques to handle deep-water high-frequency propagation using normal modes <20>.

The advantages of the normal-mode procedure are, first, that once Eq. (16) is solved we have the solution for all source/receiver configurations, and, second, that the whole solution procedure can be highly automated. In addition, the normal-mode procedure can be easily extended to slightly range-dependent environments using the adiabatic approximation where mode coupling is neglected <21-26>; numerical methods for including mode-coupling effects are present areas of research <27-31>. The disadvantages of the normal-mode solution are that conventional procedures do not include nearfield effects (the exception is Stickler's work <32>, but even there the nearfield is evaluated with a procedure similar to the FFP approach) and there are restrictions on how one can treat shear propagation in the bottom.

Both FFP and normal modes are solutions of Eqs. (5) and (6). The difference between the two is that the normal-mode method restricts the integration to horizontal wavenumbers in the interval corresponding to the discrete portion of the spectrum defined by Ineq. (18). From Eq. (20), we see that the integrand has poles at $\eta = k_n$. Hence, the function u in Eq. (10) and X_m of Eqs. (13) and (14) should have poles at the same locations.

We shall demonstrate the inter-relationship between normal mode (NM) and fast field (FFP) solutions through a numerical example using the environment given in Fig. 5. The upward-refracting sound-speed profile defines a surface duct of thickness 1500 m. We consider propagation for source and receiver both a 500 m depth, and for a frequency of 25 Hz. Two plots of the FFP integrand are shown in Fig. 6. The horizontal axis is the wavenumber (η) and the vertical axis is a normalized absolute value of the integrand amplitude. The vertical dashed line in Fig. 6a separates the discrete spectrum (defined by Ineq. 18) and the continuous spectrum. A blowup of the discrete spectrum is shown in Fig. 6b. In this particular case there are eleven propagating modes. The asterisks on the plot are the locations and the amplitudes of the modes from a NM calculation <18>. We see that the eigenvalues as calculated from the NM model (Table 1) coincide with the peaks (poles) in the FFP integrand, and also that the NM amplitudes correspond to the amplitudes of the peaks. (It turns out that this one-to-one correspondence in the amplitudes is because there is virtually no loss in this problem. Otherwise, the correspondence would not be as precise because loss shows up in the FFP calculation as widths in the peaks; nevertheless, for realistic losses the location of the poles would be the same).

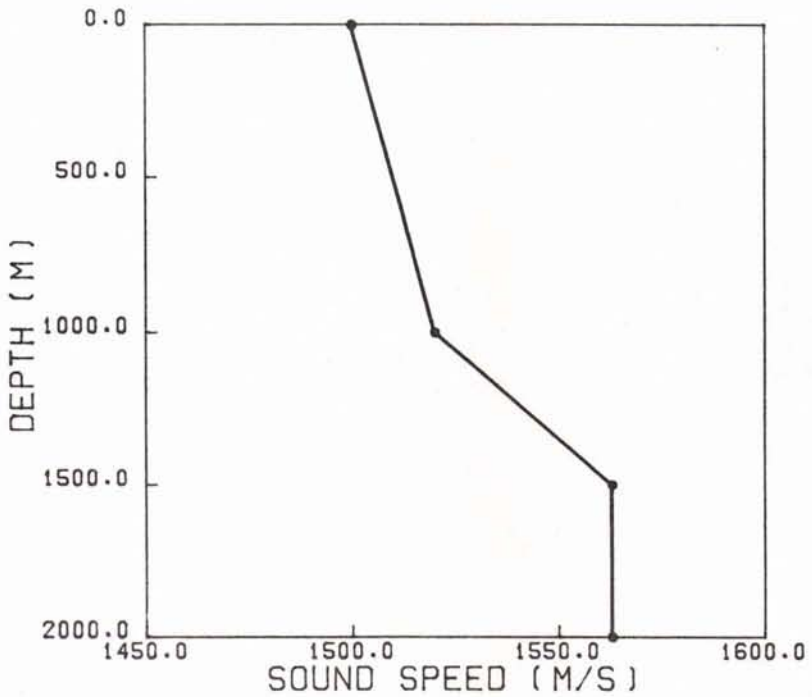

Fig. 5 Sound-speed profile for test problem

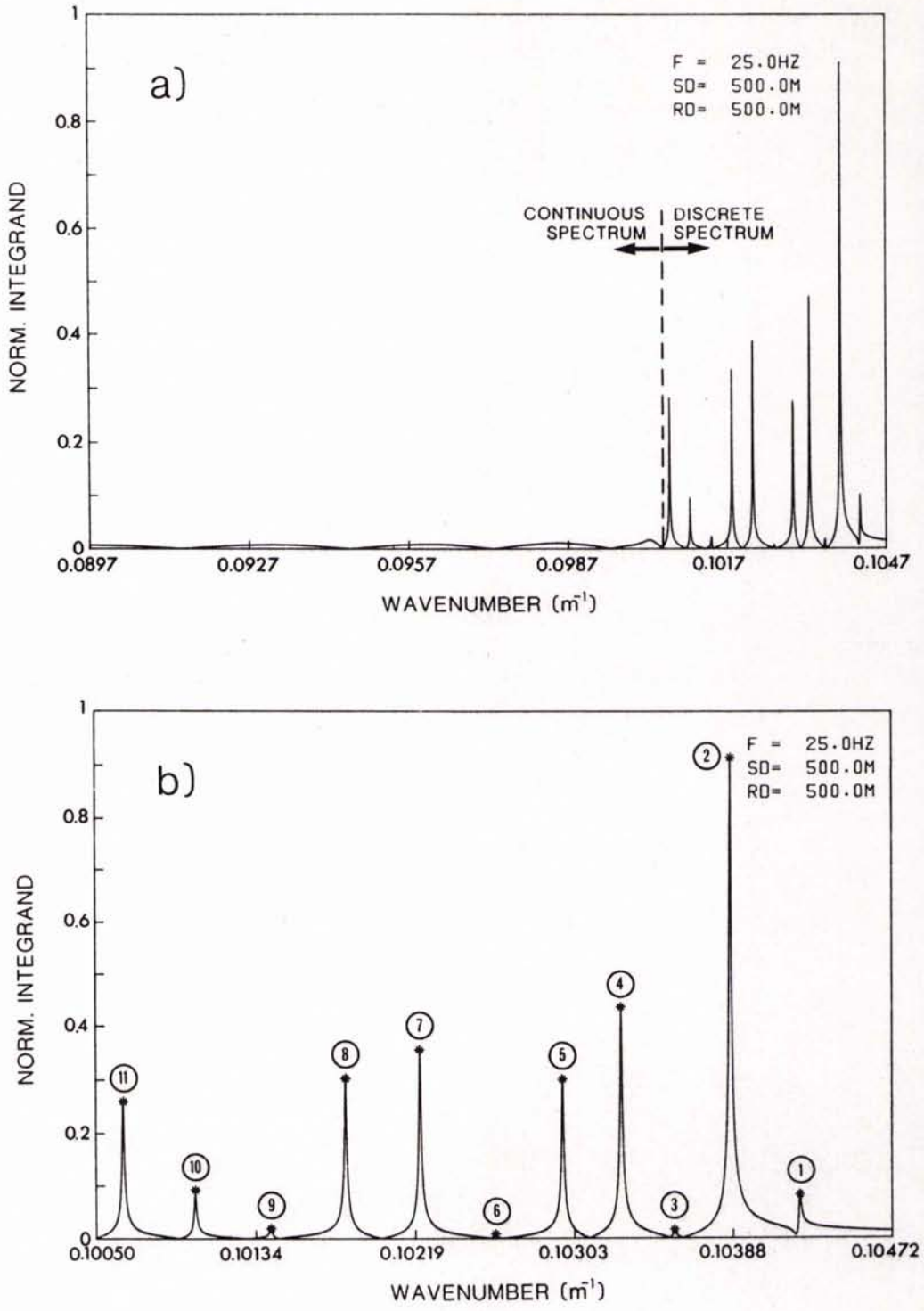

Fig. 6 FFP integrand for test problem
a) full spectrum, b) discrete spectrum

TABLE 1

MODAL EIGENVALUES

Mode no.	Wavenumber (m^{-1})
1	0.10423
2	0.10386
3	0.10356
4	0.10328
5	0.10297
6	0.10261
7	0.10221
8	0.10182
9	0.10142
10	0.10102
11	0.10064

Figure 7 displays the amplitudes of the eleven modes plotted as a function of depth. The dashed line indicates the source/receiver position. Notice the high excitation of the second mode and the low excitation of the third, sixth, and ninth modes, and notice the one-to-one correspondence with the FFP integrand shown in Fig. 6b.

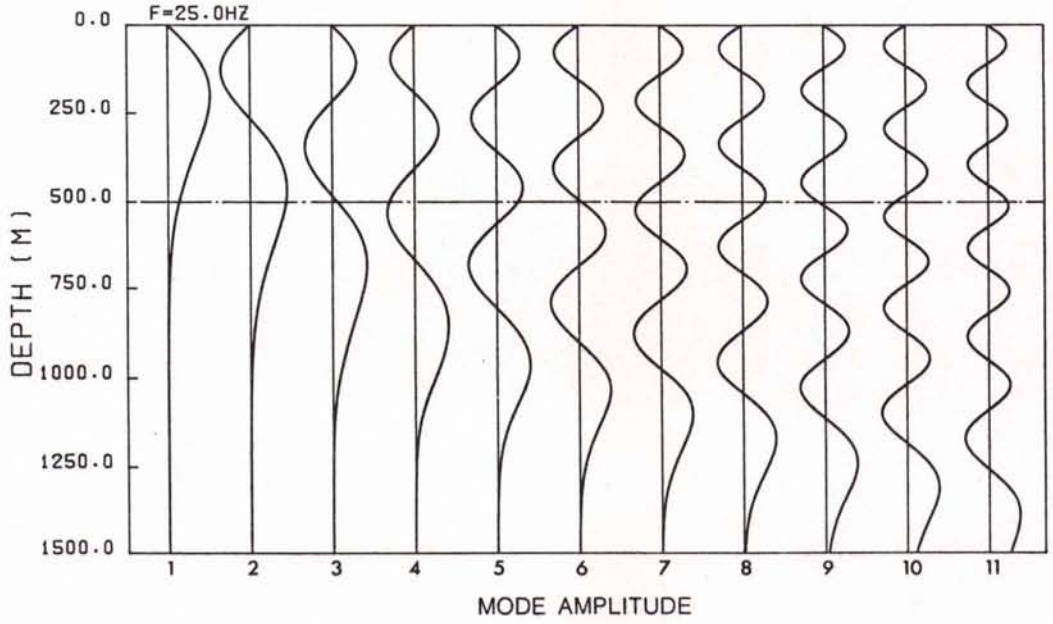

Fig. 7 Mode-amplitude functions for test problem

This particular example shows the consistency between FFP and NM calculations. In the next section we show the results on transmission loss when discrete and discrete-plus-continuous spectra are included and we compare them with calculations using the parabolic equation technique.

3.3 Parabolic equation

If the environment varies both in range and depth, the wave equation cannot be separated and therefore direct numerical integration is required. At present there are no practical methods to perform this direct integration of the three-dimensional wave equation, which is a boundary-value problem. An alternative approach is to derive an approximate wave equation that lends itself to practical numerical solution. We now outline the derivation of such an approximation, the Parabolic Equation (PE), which was introduced into underwater acoustics in 1973 by Tappert and Hardin <17,33>.

The velocity potential is decomposed as follows:

$$\phi = \psi(r,z) \cdot S(r), \tag{23}$$

and we substitute ϕ into Eq. (1) in a source-free region:

$$\psi \cdot \left[\frac{\partial^2 S}{\partial r^2} + \frac{1}{r} \frac{\partial S}{\partial r} \right] + S \cdot \left[\frac{\partial^2 \psi}{\partial r^2} + \frac{\partial^2 \psi}{\partial z^2} + \left(\frac{1}{r} + \frac{2}{S} \frac{\partial S}{\partial r} \right) \cdot \frac{\partial \psi}{\partial r} + k_o^2 n^2 \psi \right] = 0. \tag{24}$$

That is, we will eventually end up with an equation that allows a "marching-in-range" solution and we will have to initialize the solution in some way (see below). We use the notation that

$$k^2 = k_o^2 n^2, \tag{25}$$

where n is an "index of refraction" equal to c_o/c, where c_o is a reference speed.

Equation (24) may be separated into two differential equations by setting the terms in the first bracket equal to $-Sk_o^2$ and the terms in the second bracket equal to ψk_o^2, where k_o^2 is the separation constant. The functions $S(r)$ and $\psi(r,z)$ then have to satisfy the following two equations:

$$\frac{\partial^2 S}{\partial r^2} + \frac{1}{r} \frac{\partial S}{\partial r} + k_o^2 S = 0 \tag{26}$$

$$\frac{\partial^2\psi}{\partial r^2} + \frac{\partial^2\psi}{\partial z^2} + \left(\frac{1}{r} + \frac{2}{S}\frac{\partial S}{\partial r}\right) \cdot \frac{\partial\psi}{\partial r} + k_o^2 n^2\psi - k_o^2\psi = 0. \qquad (27)$$

The solution of Eq. (26) is the zeroth order Hankel function, $H_o^{(1)}(k_o r)$, whose asymptotic form has been given in Sect. 3.1. Substituting the asymptotic form of the Hankel function into Eq. (27) and making the paraxial approximation

$$\frac{\partial^2\psi}{\partial r^2} \ll 2k_o \frac{\partial\psi}{\partial r}\,, \qquad (28)$$

we obtain

$$\frac{\partial^2\psi}{\partial z^2} + 2ik_o \frac{\partial\psi}{\partial r} + k_o^2(n^2 - 1)\,\psi = 0, \qquad (29)$$

which is the parabolic wave equation.

The paraxial approximation is a narrow-angle approximation. It implies that the rapid range dependence of Eq. (23) is included in S(r), while ψ is a function varying more slowly in r. An approximation to solving Eq. (29) is to assume that n is not a function of the spatial variables but is a constant. It is shown elsewhere <33,34> that the error introduced can be made arbitrarily small by using numerical methods. With n a constant, we can fourier transform ψ with respect to z,

$$\psi(r,s) = \frac{1}{2\pi}\int_{-\infty}^{\infty} \psi(r,z)e^{-isz}dz, \qquad (30)$$

which together with Eq. (29) gives

$$-s^2\psi + 2ik_o \frac{\partial\psi}{\partial r} + k_o^2(n^2 - 1)\,\psi = 0. \qquad (31)$$

Equation (31) is a first-order differential equation with constant coefficients and has the solution

$$\psi(r,s) = \psi(r_o,s) \cdot e^{-\frac{k_o^2(n^2-1) - s^2}{2ik_o}(r - r_o)} \qquad (32)$$

where the initial condition at r_o must be specified. The field as a function of depth is the inverse transform of Eq. (30)

$$\psi(r,z) = \int_{-\infty}^{\infty} \psi(r_o,s) \cdot e^{\frac{ik_o}{2}(n^2-1)\Delta r} \cdot e^{-\frac{i\Delta r}{2k_o}s^2} \cdot e^{isz} ds \quad (33)$$

where $\Delta r = r - r_o$.

By introducing the symbol $\mathcal{F}$ for the fourier transform from the z-domain and $\mathcal{F}^{-1}$ as the inverse transform, Eq. (33) may be written as

$$\psi(r + \Delta r,z) = e^{\frac{ik_o}{2}(n^2-1)\Delta r} \cdot \mathcal{F}^{-1}\left\{ e^{-\frac{i\Delta r}{2k_o}s^2} \cdot \mathcal{F}[\psi(r,z)] \right\}. \quad (34)$$

Equation (34) is the so-called "split-step" marching solution of the parabolic equation. The fourier transforms are performed using an FFT. It is the solution for n constant, but the error introduced when n (profile and bathymetry) varies with range and depth can be made arbitrarily small by increasing the transform size and decreasing the range-step size <33,34>.

The parabolic equation is not a boundary-value equation as we have numerically formulated it above. We can include the surface boundary condition by taking an anti-symmetric FFT about the sea surface (z = 0). In practice this is performed by taking sine transforms. The boundary conditions in the bottom are simulated by including the discontinuity in velocity in the sound-speed profile. There are methods to also include the density discontinuity <33>. The radiation condition as z goes to infinity is simulated by requiring the field to exponentially tail off for large values of z beyond which there would not be any significant acoustic interaction.

As mentioned above, the PE method requires an initial starting solution. Two methods have been used for describing a point source. The first method is to initialize the field with a set of normal modes descriptive of the point source in the starting environment. This would not include the continuous portion of the spectrum (see Sect. 3.2), but for long-distance propagation this approximation is adequate. A second approach has proved to be simpler and as effective. The point source is approximated by two gaussians that are anti-symmetric about the sea surface, thereby automatically including the pressure-release boundary condition at the surface. Both starting techniques have been used in this paper. We will see that by using the gaussian starting field part of the continuous spectrum is included in the PE solution.

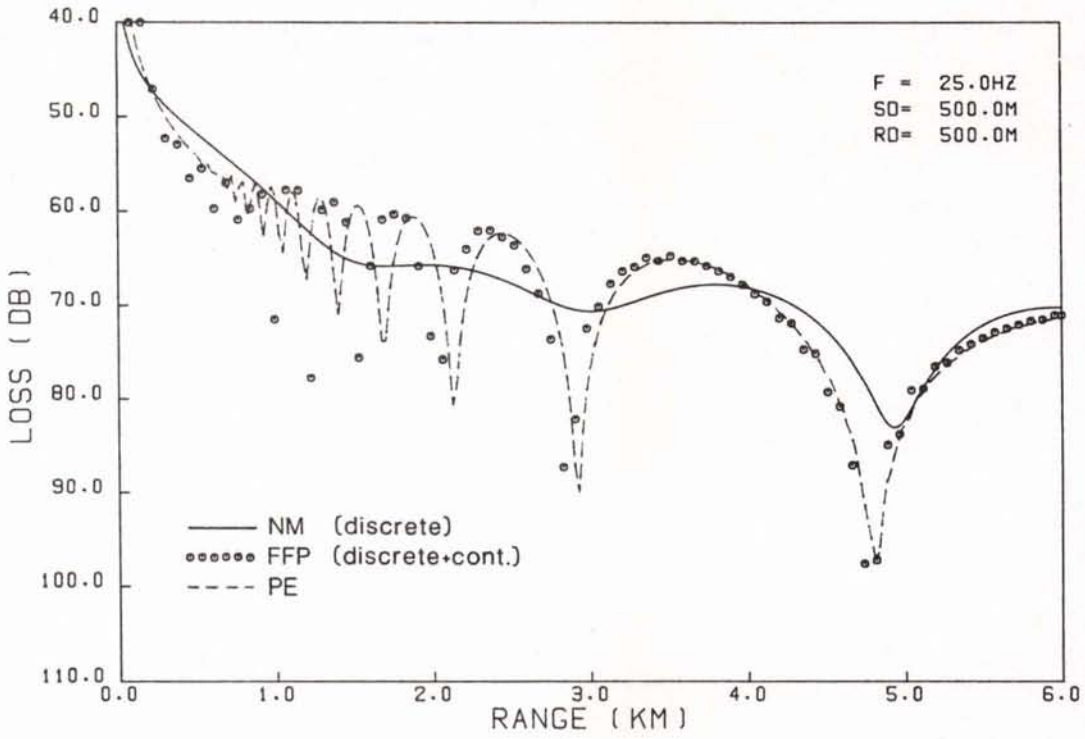

Fig. 8 Computed transmission losses for test problem

In Sect. 3.2 we compared FFP and NM, using a simple environment (Fig. 5) as an example. We now look at transmission loss from the point of view of discrete, discrete-plus-continuous, and PE, which does not obviously distinguish between regions in the spectrum. Figure 8 shows computed transmission loss from 0 to 6 km, defined as TL = -20 log (P/P_1), where P_1 is the pressure amplitude at 1 m distance from the source. Note that the PE tracks the FFP results in the nearfield indicating that at least part of the continuous portion of the spectrum is included in the PE calculation when using a gaussian starting field. We can also see how the three model results converge in the farfield; recall that the NM calculation does not include the full nearfield contribution. This particular example clearly illustrates the consistency and inter-relationship between the three models.

The advantages of the PE are that it handles a range-dependent environment and gives the acoustic field in the entire water column without additional computational effort. Its disadvantages are that the procedure is not easily automated, and it is practical only for low-frequency propagation since computation times increase with frequency squared. Moreover, there is no straightforward way of handling shear propagation in the bottom.

The parabolic wave equation as given by Eq. (29) is based on the paraxial approximation, and hence only propagation close to the horizontal (± 20°) is accurately handled. This angle limitation is of minor importance for a wide class of ocean acoustics problems. However in studying bottom-interacting propagation, the narrow-angle approximation becomes a serious limitation. It has recently been shown <35,36> that a slight modification to Eq. (20) can improve the angle coverage to ± 40°, yielding a modified parabolic equation, which, however, can no longer be solved by the split-step technique. Instead finite-difference solution techniques have been applied <35,37>, and a working computer code is already available <38>.

Numerical PE results given in this paper were all done with a model based on the standard parabolic equation technique as delineated above.

3.4 Ray theory

This paper is concerned mainly with wave theory; nevertheless, for completeness, we include a brief description of ray theory. In this case we assume a solution of Eq. (1) (with right-hand side equal to zero) as

$$\phi = \psi(x,y,z) \cdot e^{iS(x,y,z)}. \tag{35}$$

$S(x,y,z)$ is a phase function that includes rapid variations as a function of range, and $\psi(x,y,z)$ is a more slowly varying envelope function in which geometrical spreading and loss mechanisms are included (in the PE, S contains the cylindrical spreading factor). Substituting Eq. (35) into the wave equation and separating real and imaginary parts, we obtain

$$\frac{1}{\psi}\nabla^2\psi - (\nabla S)^2 + k^2 = 0, \quad 2(\nabla\psi \cdot \nabla S) + \psi\nabla^2 S = 0. \tag{36}$$

We now make the geometrical-acoustics approximation

$$\frac{1}{\psi}\nabla^2\psi << k^2, \tag{37}$$

that is, the amplitude of the phase function varies slowly in range with respect to wavelength. Substituting Eq. (37) in Eq. (36) gives the eikonal equation,

$$(\nabla S)^2 = k^2. \tag{38}$$

The trajectory of the rays is perpendicular to the surfaces of constant phase (wavefronts), S, and is expressed by

$$\frac{d}{d\ell}\left\{k\frac{d\vec{X}}{d\ell}\right\} = \nabla k, \qquad (39)$$

where ℓ is the arc length along a ray and X is the coordinate. It can be shown that the direction of the average energy flow is along these trajectories and the amplitude of the field at any point can be obtained from the density of these rays; formally, having solved for S, the amplitude is obtained from solving the second part of Eq. (36). We also mention here that corrected ray theory assumes that ψ is a function of frequency and an expansion in powers of inverse frequency is made, the leading term being the infinite-frequency solution with the additional terms being corrections from the infinite-frequency solution.

The advantages of ray theory methods are that the computations are rapid and that ray traces give a very physical picture of the acoustic paths. The disadvantage is that ray-theory is an infinite-frequency approximation and therefore does not include diffraction and other wave effects. This shortcoming also prevents ray theory from adequately describing significant bottom interaction and low-frequency ducted propagation.

4 NUMERICAL MODELS: THEIR APPLICABILITY AND CONSISTENCY

The four acoustic models described in this paper are a representative subset of the many different propagation models in use in underwater acoustics today. The reason for developing new models is to obtain either more accurate solutions or faster solutions to specific problems. Each model has its area of applicability depending on the theoretical limitations in the model and on the numerical efficiency of the computer code.

MODEL TYPE	APPLICATIONS							
	SHALLOW WATER				DEEP WATER			
	LF		HF		LF		HF	
	RI	RD	RI	RD	RI	RD	RI	RD
RAY								
NORMAL MODE								
FAST FIELD (FFP)								
PARABOLIC EQ.(PE)								

LF: LOW FREQUENCY (< 500 Hz) RI: RANGE-INDEPENDENT ENVIRONMENT
HF: HIGH FREQUENCY (> 500 Hz) RD: RANGE-DEPENDENT ENVIRONMENT

Fig. 9 Applicability of four propagation models

To indicate with some precision the type of ocean environment for which a given model should be used, we have classified environments according to water depth, frequency, and environmental complexity, as shown in Fig. 9. Here shallow water indicates all water depths for which sound interacts significantly with the ocean bottom. The separation frequency of 500 Hz between the low- and high-frequency regimes is arbitrarily chosen.

When indicating the applicability of a propagation model to a given type of environment we take into consideration limitations in the underlying theory. Ray models are applicable mainly to high-frequency propagation. Only ray and PE models accurately handle a range-dependent environment. The normal-mode model treats range dependence in the adiabatic approximation. When indicating a model's practicality we consider exclusively the computation time, which, of course, depends on the required accuracy. The computation time increases with both frequency and water depth for wave models (mode, FFP, PE), while the time is relatively independent of these parameters for the ray models. Likewise, computation time is proportional to the number of profiles in a range-dependent environment for both ray and mode models, while a PE model takes essentially the same time for range-dependent and range-independent environments.

Full-box shading in Fig. 9 means that a model is applicable as well as practical. On the other hand, if a box is only partially shaded, it means that the model is applicable with caution (theoretical limitations), or that computation times are excessive. The above judgements are, of course, relative. For instance, in our first evaluation some columns contained no applicable models. In these columns we therefore selected the model we felt was the most practical end denoted it by a fully shaded box. For a column where more than one box is fully shaded, the choice of model will depend on the actual models on hand, the running time, input/output options available, etc.

Since the various models are approximate solutions of the wave equation, it is valuable to check the validity of these approximations by doing an inter-model comparison for situations where all four models are considered applicable. Returning to Fig. 9, we note that all models should handle a range-independent shallow-water environment at around 500 Hz, even though the mode and FFP models are designated most applicable (fastest).

An example of a transmission loss computation for shallow water is given in Fig. 10. Here an isovelocity water column (1500 m/s) is 100 m deep and both source (SD) and receiver (RD) are at mid-depth. The bottom is considered homogeneous, with a sound speed of 1550 m/s, a density of 1.2 g/cm^3, and an attenuation of 1 dB/wavelength. We see from Fig. 10 that the three

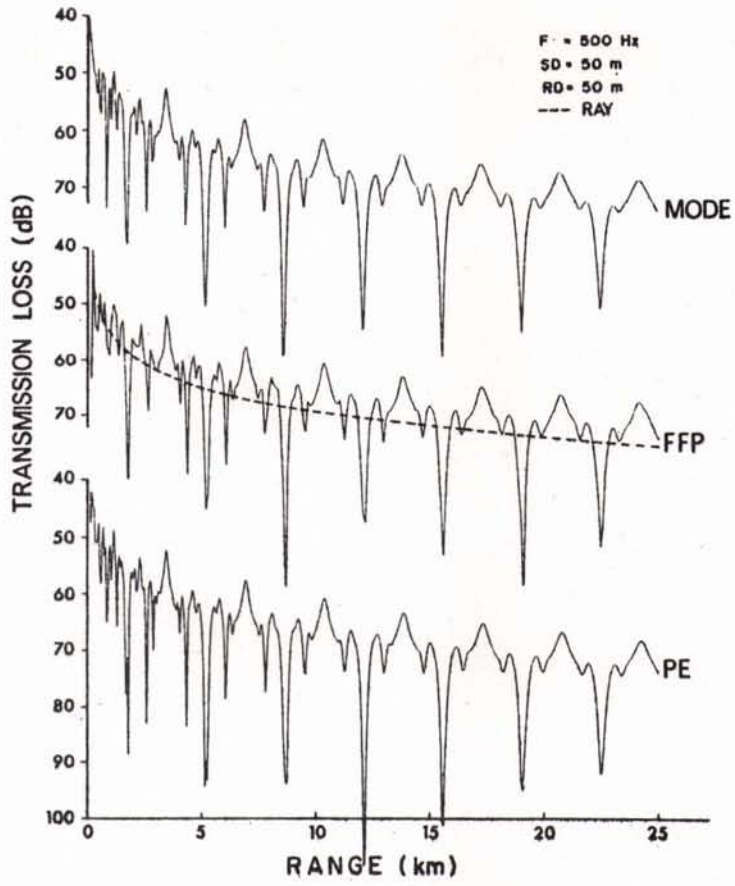

Fig. 10 Inter-model comparison for shallow-water environment

wave models (mode, FFP, PE) give virtually identical results both for level and for the multipath interference structure as a function of range. The ray model, though it cannot reproduce the interference pattern, does yield the same approximate level (dashed line).

Many consistency tests of acoustic models have to be carried out in order to check the complex computer programs within the framework of the theoretical limitations particular to each model <39>. A positive outcome of an inter-model comparison helps us to gain confidence in particular numerical models. However, we should remember that the final check on an acoustic model is a comparison with experimental data. This demonstrates whether or not the model includes all the physics necessary for explaining and understanding sound propagation in a real ocean environment. A series of model/data comparisons can be found in <40-43>.

5 SPECIAL MODEL APPLICATIONS

This section is dedicated to a study of some general wave-propagation problems, for which illustrative numerical solutions can be obtained in a straightforward manner using one of the aforementioned ocean-acoustic models. We shall first address the problem of reflection of a gaussian beam of arbitrary width at a fluid/solid interface near the Rayleigh angle, where a leaky surface wave is excited causing a complex reflection pattern with beam splitting and beam displacement. This is a well-researched problem in both optics and acoustics, which we can easily solve with the fast-field program. Next we study propagation in range-dependent waveguides using the parabolic equation technique. We shall address acoustic radiation from a duct into free space as well as mode coupling in tapered waveguides.

5.1 Beam reflection at fluid/solid interface

Bounded beam reflection near a critical angle is a subject that has received considerable attention in the past, both within the field of electromagnetics <44-48> and acoustics <49-55>. The phenomenon of interest has mainly been the displaced reflected beam, while the transmitted field has been studied in much less detail. There are basically two different wave phenomena that can account for the observed features of the reflected field. One is the excitation of a lateral wave at the interface when a beam of finite width is incident on the interface at grazing angles lower than the critical angle. The reflected field is then composed of contributions from both the specular reflection and the lateral wave field, causing an apparent lateral displacement of the reflected beam. In acoustics, the lateral wave phenomenon is associated with beam reflection at fluid/fluid interfaces.

The second phenomenon is associated with the excitation of a leaky surface wave, which again complicates the reflection pattern when added to the specularly reflected field. This phenomenon occurs in acoustics when a bounded beam is incident on a fluid/solid interface just below the shear critical angle.

Various aspects of bounded beam physics have been studied theoretically as well as experimentally in the past 35 years. The lateral displacement of a reflected light beam was first observed by Goos and Hänchen <44>, and the phenomenon is therefore often referred to as the Goos-Hänchen effect. Several theoretical papers have addressed the beam reflection problem, for instance <45-49>, though always with some theoretical limitations, such as beamwidth large compared to the wavelength, lossless media, parallel beams of particular shape (gaussian), etc.

We shall here apply the fast-field program (FFP) to numerically solve the reflection problem, and, as we shall see, this

technique treats the complete problem without any of the above limitations. We are going to study reflection at a fluid/solid interface, where the reflection phenomenon is associated with the excitation of a leaky surface wave (Rayleigh wave). However, the FFP model could as well be applied to reflection and transmission for a solid plate in a liquid <52-53> or to the transmission through a fluid/fluid boundary <54-55>.

The FFP model <13> provides an exact numerical solution for the acoustic field generated by a point source in a multilayered fluid/solid environment (Sect. 3.1). Wave attenuation for both compressional and shear waves is included in the theory. We have modified the standard code to efficiently solve the system of equations for a number of point sources, equidistantly spaced and forming a vertical line array. The total acoustic field is found by superposition of the contributions from individual point sources. Hence, in this model the beam is generated by a vertical source array, and the beam direction is varied by appropriately phasing the source elements. By using a gaussian amplitude weighting across the array, a gaussian beam can be generated, propagating at any angle with respect to the horizontal. By varying the array distance from the interface and the number of source elements (half-wavelength spacing), a beam of arbitrary width can be generated, and we can obtain parallel, diverging, or converging beams, as we wish. Hence, the model is very general in concept, and should handle the reflection problem accurately for any beamwidth and for multilayered systems (plates) as well as the reflection and transmission at a single fluid/solid interface. The solution is for a plane geometry, i.e. a two-dimensional beam.

We first consider computational results for a water/steel interface. Information on material parameters were taken from Breazeale et al <51>, and the FFP results will be compared with the theory of Bertoni and Tamir <47>, here named the BT theory. Results for reflection at the Rayleigh angle (59.35°) are given in Fig. 11 for two different beamwidths.

Computations were done at 20 kHz, and the acoustic field is displayed as iso-loss contours given in arbitrary decibels (low values correspond to high intensity). We are considering incoming parallel gaussian beams, where the beamwidth is 10 and 64 wavelengths respectively. Note in Fig. 11a that the narrow beam, when reflected, is being split up in two beams separated by a "null strip". The beam to the left is displaced slightly backwards, while the rightmost beam is displaced forwards 18 wavelengths. This behavior is in complete agreement with the BT theory. With increasing beamwidth, the energy shifts to the forwardly displaced beam, and we end up (Fig. 11b) with a single-beam reflection with a displacement of 50 wavelengths. The general behavior seen in these examples is predicted by Bertoni and Tamir, and the measured

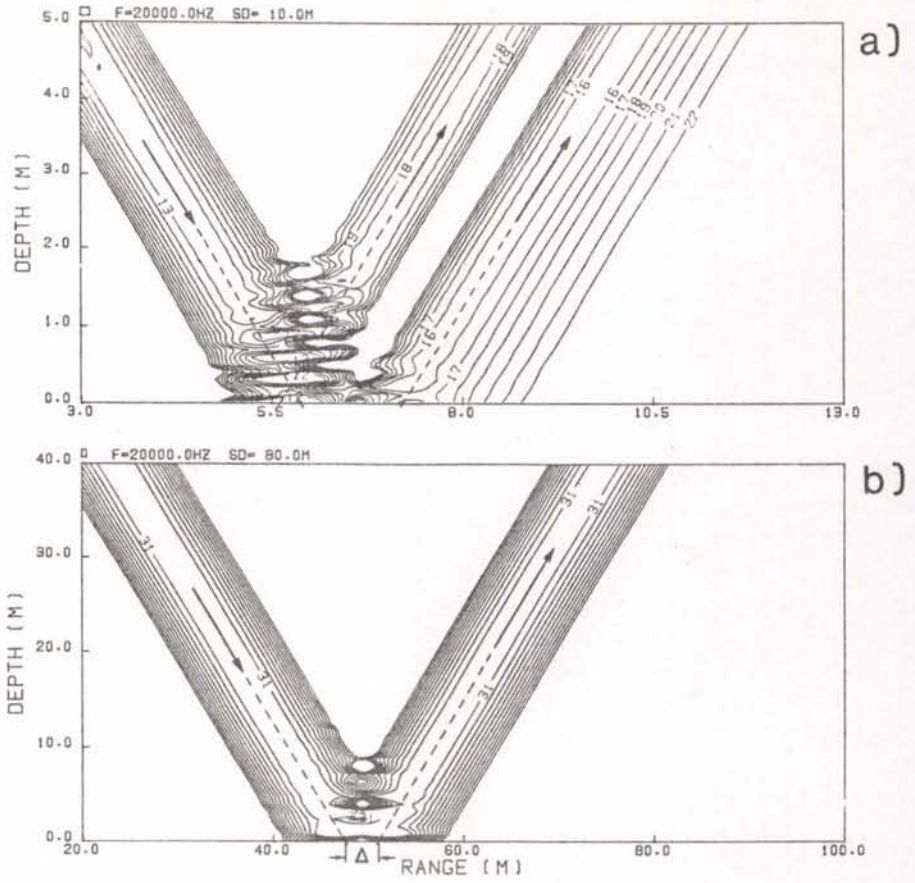

Fig. 11 Beam reflection at water/steel interface at the Rayleigh angle.
a) narrow beam of width 10λ,
b) broad beam of width 64λ.

displacement versus beamwidth gives data points that fall exactly on the displacement curve computed from the BT theory.

A more challenging investigation was to explain the disagreement between theory (BT) and experimental results for aluminium oxide, as reported by Breazeale et al <51>. We proceed to calculate the Rayleigh-wave properties for a water/aluminium-oxide interface using the material parameters given in <51>. For a water speed of 1490 m/s, a frequency of 2 MHz, and with realistic attenuation coefficients in both media, we found the leaky surface wave to have a phase velocity of 5825.6 m/s corresponding to an angle of 75.18°. The leakiness of the surface wave is given by the imaginary part of the wave number, which is calculated to be 23.3 m^{-1}. These Rayleigh-wave properties were determined from a separate computer code that finds the poles for the complex reflection coefficient.

The next step was to generate a parallel beam (plane wave front) with a half-width of 16.6 mm as used in the experiment. The computed field at the Rayleigh angle is shown in Fig. 12. Again we see that the reflected beam is split in two, and we also notice the leading radiated field associated with the surface wave. In fact, full information about the Rayleigh wave can be read off directly from the rightmost contour lines (46 to 54 dB). They have a slope of 75.2° with the horizontal (the Rayleigh angle), and the field decay is 23.3 Nepers/m (the imaginary part of the wavenumber). We found that this property of the reflected field is independent of the angle of incidence of the incoming beam, and, as we shall see, it is a valid criterion for determining the Rayleigh-wave properties also for a diverging beam.

The computed intensity distribution in the reflected beam is given in Fig. 13, normalized with the amplitude of the incoming beam measured at the interface (dotted profile at 75.2°). The vertical dashed line corresponds to the position of a specular reflection. The results are computed 40 cm above the interface, corresponding to a horizontal cut through the contour plot (outside the frame). Hence, this display differs slightly from the experimental results, which were obtained measuring perpendicular to the beam direction. This difference is however minor at these angles. We see from Fig. 13 the expected behavior, i.e. a single specularly reflected beam when moving 1.5 to 2.0° away from the Rayleigh angle. We also notice that the interference null is strongest at the Rayleigh angle (75.2°) as predicted by the BT theory for parallel beams. Hence these results confirm that the Rayleigh angle for the chosen material parameters is 75.2°.

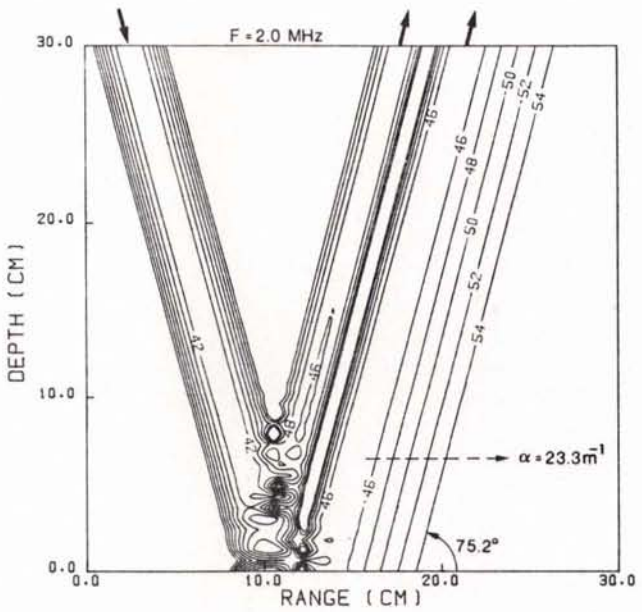

Fig. 12
Reflection of parallel beam at water/aluminium-oxide interface

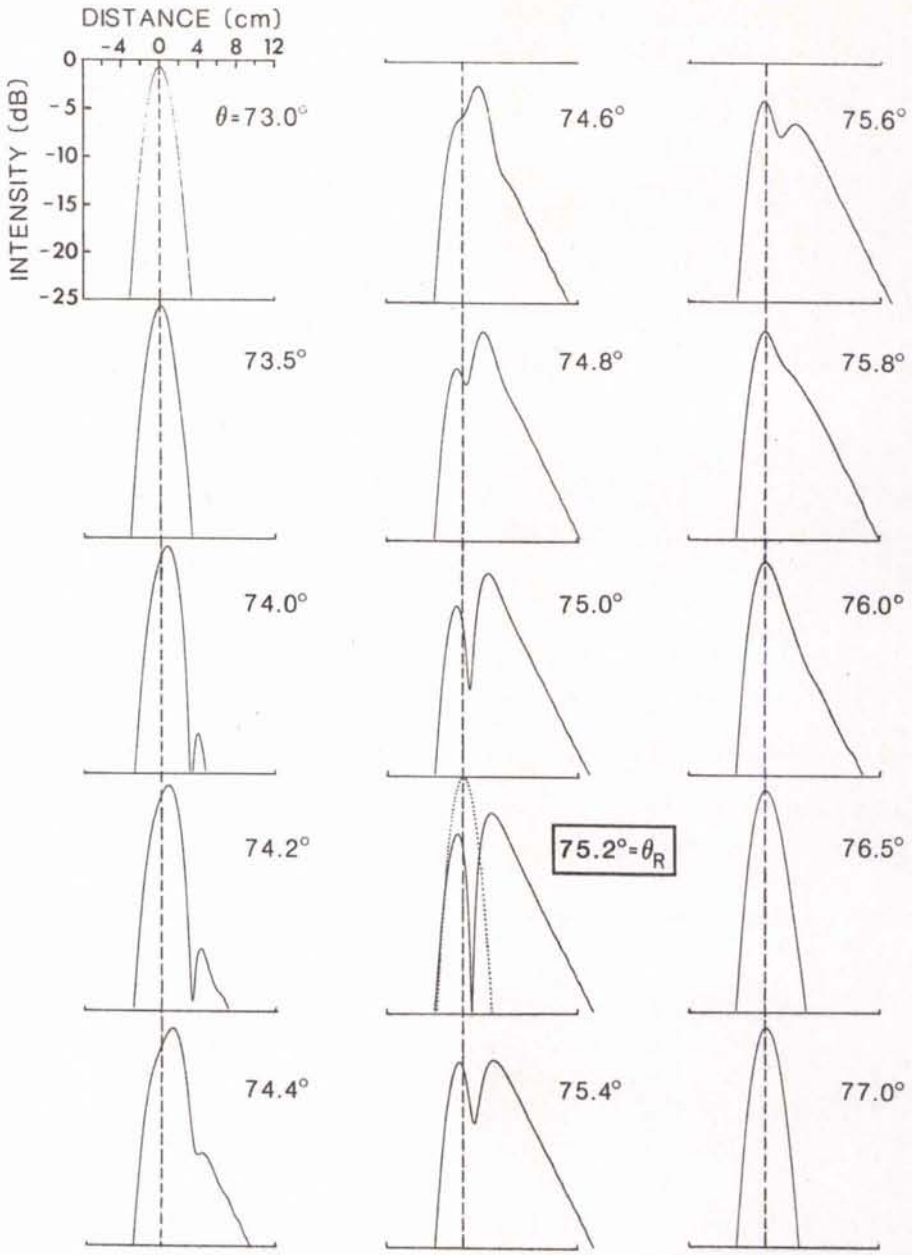

Fig. 13 Reflectivity pattern versus grazing angle for parallel beam incident on a water/aluminium-oxide interface

We now consider a slightly diverging beam (curved wave front) as actually used in the experiment. The beamwidth is again 16.6 mm, and the divergence measured at the 3 dB down-points is 2.7° at the interface. Our results for the reflected field at the Rayleigh angle is given in Fig. 14. We notice that the reflected field is now much more complicated, with essentially 3 reflection peaks. However, the undisturbed leading edge of the radiated surface wave exhibits the same properties as before, i.e. the isointensity contours have a slope of 75.2° with the horizontal, and the field decay is 23.3 Nepers/m parallel to the interface.

The computed field intensity 40 cm above the interface is given in Fig. 15 as a function of the incoming beam angle. We notice the many interference lobes now present in the reflected beam. In this case the reflection pattern at the Rayleigh angle (75.2°) has no particular features, such as a pronounced interference null, that makes it possible to easily determine the Rayleigh angle. In fact, when searching for the strongest interference null, one finds this to occur at approximately 75.8°, which is very close to the angle (75.7°) designated the Rayleigh angle in the experiment <51>, using the above (wrong) criterion. Hence, we may conclude from this set of curves, that an experimental verification of the Rayleigh angle can most easily be done by measuring the slope of the isoloss contours in the undisturbed leaky wave field as seen on the contour plots.

A detailed comparison between our theoretical result at 75.8° and the experimental result given in Ref. <51>, shows a clear improvement over the prediction obtained from the BT theory. However, some disagreement on peak levels still exists, which we

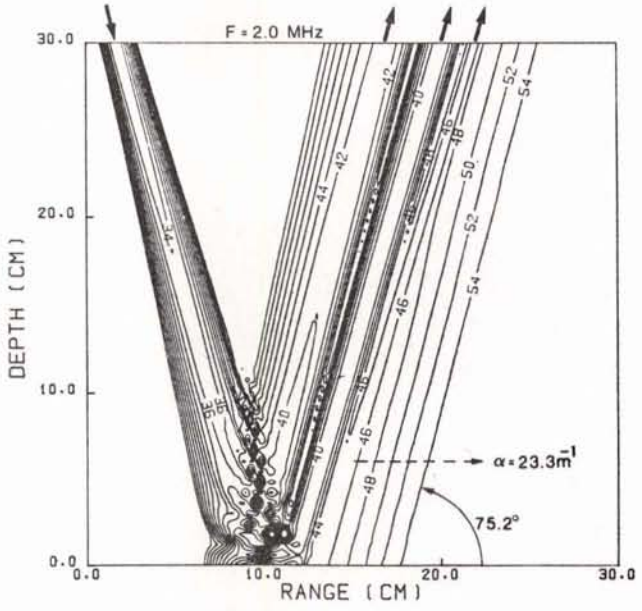

Fig. 14
Reflection of diverging beam at water/aluminium-oxide interface

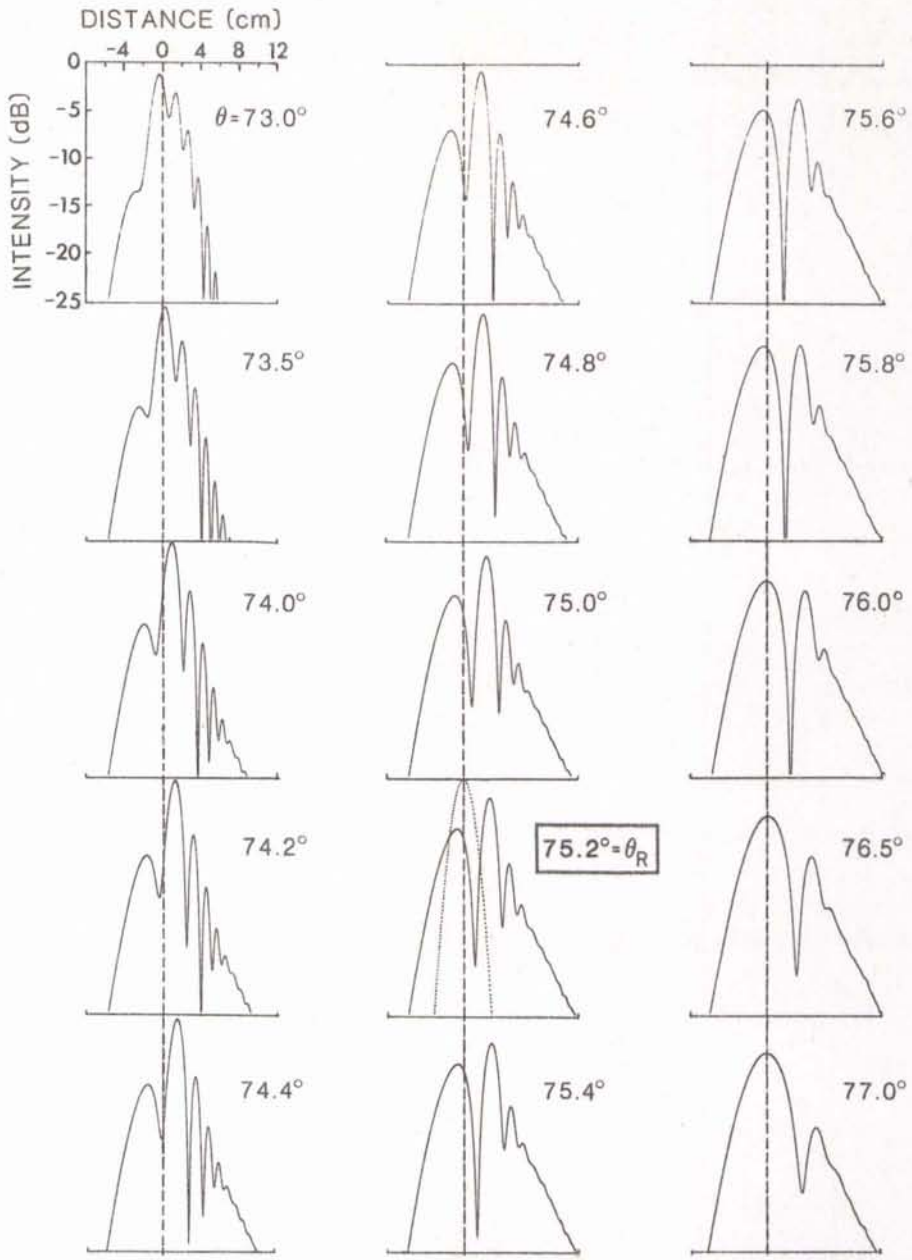

Fig. 15 Reflectivity pattern versus grazing angle for diverging beam incident on a water/aluminium-oxide interface

speculate could be due to inaccurate knowledge of the material parameters for aluminium oxide.

The beam reflection calculations with the FFP model is an ongoing project. We are mainly interested in studying the reflection process for very narrow (focused) beams, where the reflection process is strongly influenced by diffraction effects.

5.2 Propagation from duct into free space

The study of sound propagation in a range-dependent environment is a fascinating subject, to which we will devote the remainder of this paper. We have chosen to solve a series of relatively simple propagation situations suitable for the parabolic equation technique. As pointed out in Sect. 3.3, the PE method is limited to propagation within ± 20° with respect to the horizontal, and back-scattering is neglected in the solution. The PE calculations have been done for a cylindrical geometry.

One of the simplest range-dependent problems in acoustics is the radiation of sound from a symmetric duct into free space. PE solutions to this problem are shown in Fig. 16. The duct is 100 m wide with a sound speed of 1500 m/s and a density of 1 g/cm^3. The infinitely thick duct wall has a speed of 1550 m/s. There is no density change in the problem, and material losses are neglected. At a frequency of 50 Hz, there are two propagation modes in the duct.

Figure 16a shows the computed field from a source placed in the middle of the duct. In this case only the symmetric 1st mode is excited, radiating symmetrically into free space beyond a range of 2 km. The initial modal field for the PE calculation was supplied by a normal-mode model. Next we moved the source to a depth of 27 m below the center of the duct, which gives equal excitation of the two modes. Figure 16b shows that the radiated field is now split up into two almost symmetric beams. We would expect the radiated field to be determined by the field distribution across the duct opening. This is confirmed in Fig. 16c, where the duct has been truncated at 1.5 km range; we now obtain an asymmetric radiation pattern with most of the energy being contained in the down-going beam.

The above numerical results provide considerable physical insight into the duct radiation problem. The examples were chosen so as to facilitate a physical interpretation of the contour plots. However, more complex situations could easily be investigated.

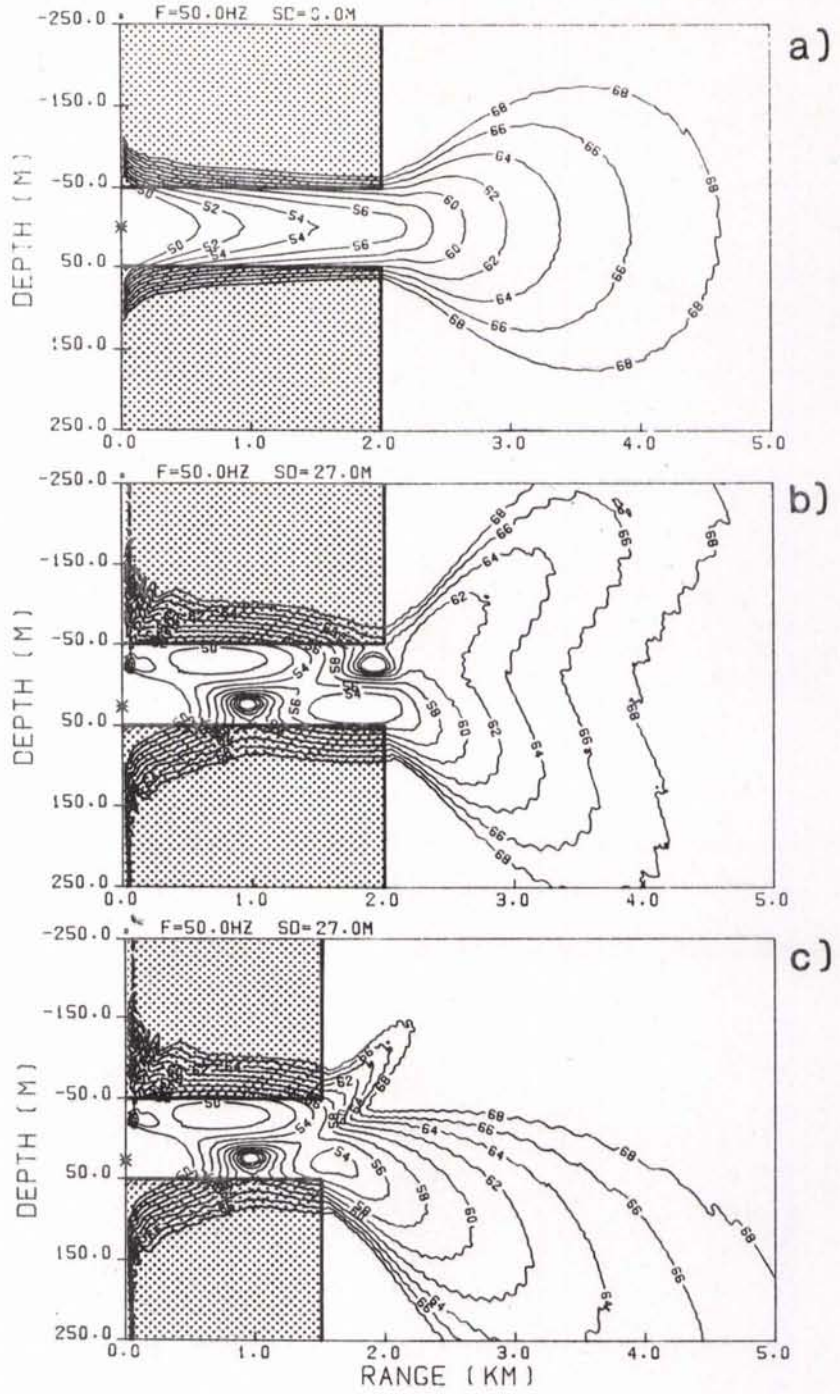

Fig. 16 Sound radiation from duct into free space
a) one symmetric mode excited in duct,
b) two modes excited in duct,
c) as b) but for a shorter duct.

5.3 Up-slope propagation

We now proceed to study propagation over sloping bottoms at a sufficiently low frequency that phenomena such as mode cutoff and mode conversion can be investigated in some detail. First we consider up-slope propagation for the environment given in Fig. 17. The water/bottom interface is indicated on the contour plot by the heavy line starting at 350 m depth and moving towards the surface beyond a range of 10 km. The bottom slope is 0.85°. The frequency is 25 Hz and the source depth is 150 m. The water is taken to be isovelocity with a speed of 1500 m/s, while the bottom is characterized by a speed of 1600 m/s, a density of 1.5 g/cm^3, and an attenuation of 0.2 dB/wavelength.

Before interpreting the contour plot, let us have a look at the simplified sketch in the upper part of Fig. 17. Using the ray/mode analogy, a given mode can be associated with up- and down-going rays with a specific grazing angle corresponding to a given mode. As sound propagates up the slope, the grazing angle for that particular ray (mode) increases, and at a certain point in range the angle exceeds the critical angle at the bottom, meaning that the reflection loss becomes very large and that the ray essentially leaves the water column and starts propagating in the bottom. The point in range where this happens corresponds to the cutoff depth for the equivalent mode.

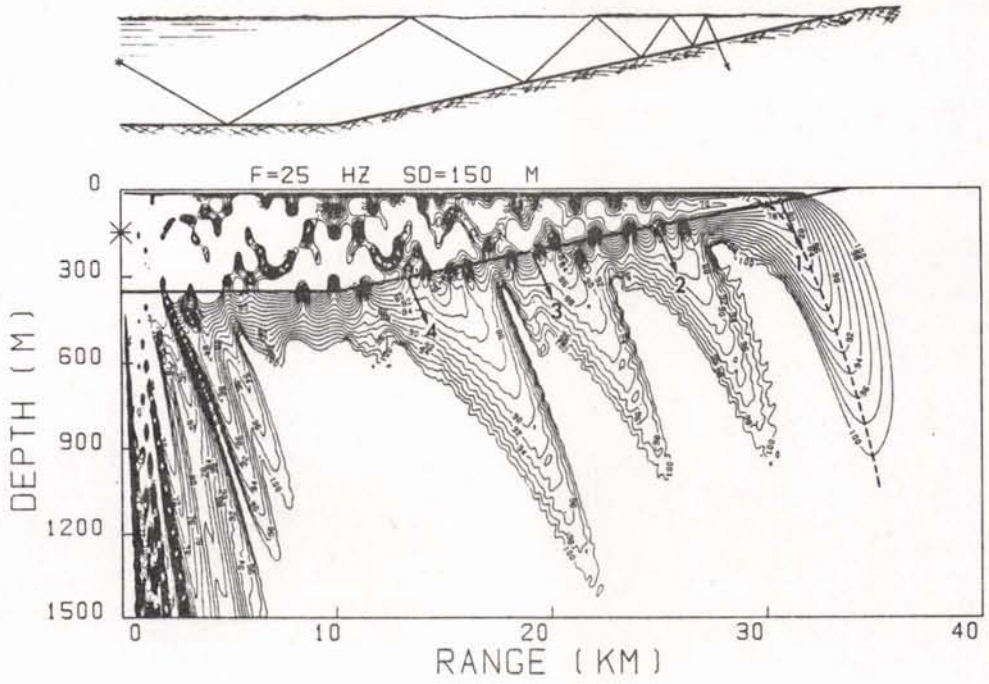

Fig. 17 Up-slope propagation showing discrete mode cutoffs

To emphasize the main features in Fig. 17, we have chosen to display contour levels between 70 and 100 dB in 2 dB intervals. Thus high-intensity regions (loss < 70 dB) are given as blank areas within the wedge, while low-intensity regions (loss > 100 dB) are given as blank areas in the bottom. The PE solution was here started off by a gaussian initial field, and there are four propagating modes. The high intensity in the bottom at short ranges (< 10 km) corresponds to the radiation of "continuous modes" into the bottom. As sound propagates up the slope we see four well-defined beams in the bottom, one corresponding to each of the four modes. This phenomenon of energy leaking out of the propagation channel as discrete beams has been confirmed experimentally <56>, and a detailed study of this phenomenon using the PE method has been reported elsewhere <57>.

This particular example of mode coupling where discrete modes trapped in the water column couple into "continuous" modes propagating in the bottom, has received much attenation recently; several theoretical papers <31> and <58-60> have appeared offering solutions to the wedge-propagation problem.

We now proceed to study the problem of mode coupling within the wedge itself. Strong coupling can be achieved either by increasing the bottom slope or by increasing the frequency. It is the latter case that will be considered here. Figure 18 shows PE calculations for a simple wedge problem. The initial water depth is 100 m and the bottom slope is 2°. The water is taken to be isovelocity with a speed of 1500 m/s, while the bottom has a speed of 1550 m/s. There is no density change in the problem, and material losses are neglected. The source depth is 50 m, and the initial field for the PE calculation was supplied by a normal-mode model. The two plots are for source frequencies of 50 and 500 Hz, respectively. In both cases, only the first mode was propagated up the slope.

We notice in Fig. 18a that no mode coupling takes place at a frequency of 50 Hz. The contour lines are smooth, indicating that the local mode at range zero adapts to the changing water depth until it reaches the cutoff depth, where the energy radiates into the bottom. This is an example where propagation is well described by adiabatic mode theory <21-26>.

Strong mode coupling occurs when we increase the frequency to 500 Hz (Fig. 18b). The field within the wedge becomes complicated, and so does the radiation pattern into the bottom. We have done no attempt to analyse this complex mode-coupling problem in detail, but the PE technique could certainly be used for such a study.

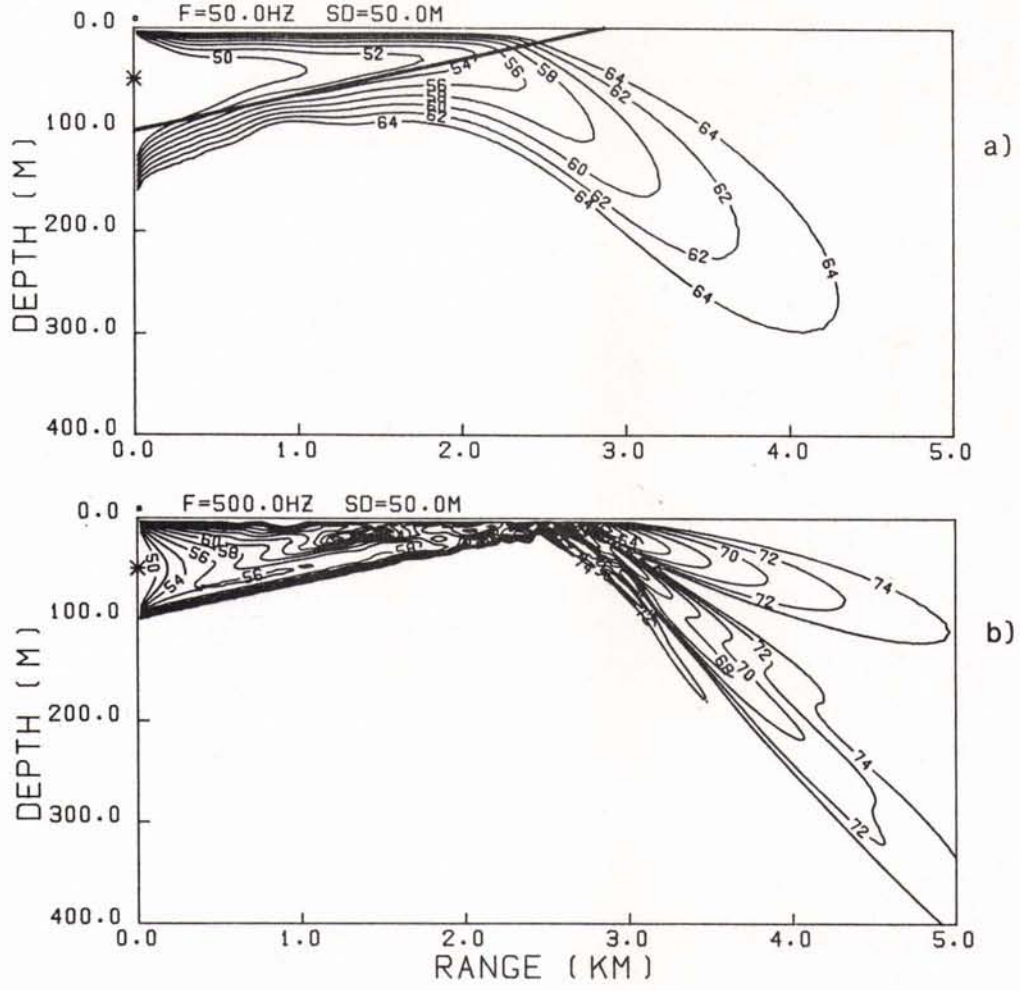

Fig. 18 Up-slope propagation over a constant 2° slope
a) 50 Hz, no mode coupling,
b) 500 Hz, strong mode coupling.

5.4 Down-slope propagation

We now consider the problem of down-slope propagation as illustrated in Fig. 19. The initial water depth is 50 m and the bottom slope is 5°. The water column is isovelocity with a speed of 1500 m/s, while the bottom has a speed of 1600 m/s. The density ratio between bottom and water is 1.5, and a wave attenuation of 0.5 dB/wavelength has been included in the bottom. The two contour plots are for source frequencies of 25 and 500 Hz, respectively. The initial fields for the PE calculations were supplied by a normal-mode model, and, in both cases, only the first mode was propagated down the slope.

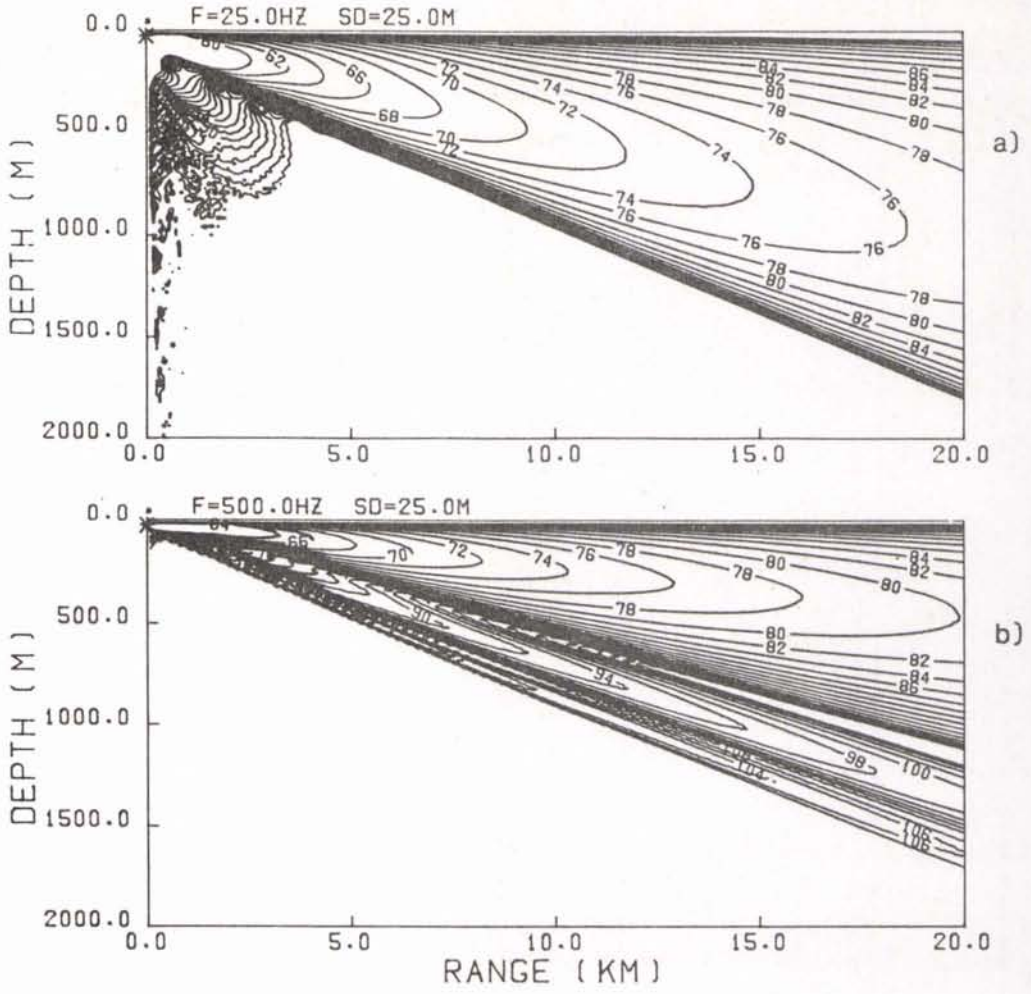

Fig. 19 Down-slope propagation over a constant 5° slope
a) 25 Hz, no mode coupling,
b) 500 Hz, strong mode coupling.

Fig. 19a shows that some energy propagates straight into the bottom at short ranges (coupling into the continuous spectrum). However, beyond the nearfield, propagation within the wedge is clearly adiabatic with the one propagating mode adapting well to the changing water depth. At range 20 km the energy is entirely contained in the local first mode, even though as many as 21 modes can exist in a water depth of 1800 m.

By increasing the frequency to 500 Hz (Fig. 19b), strong mode coupling occurs within the wedge. At long ranges, two interference nulls are present in the energy distribution over depth indicating that the energy is now partitioned among a few lower-order modes.

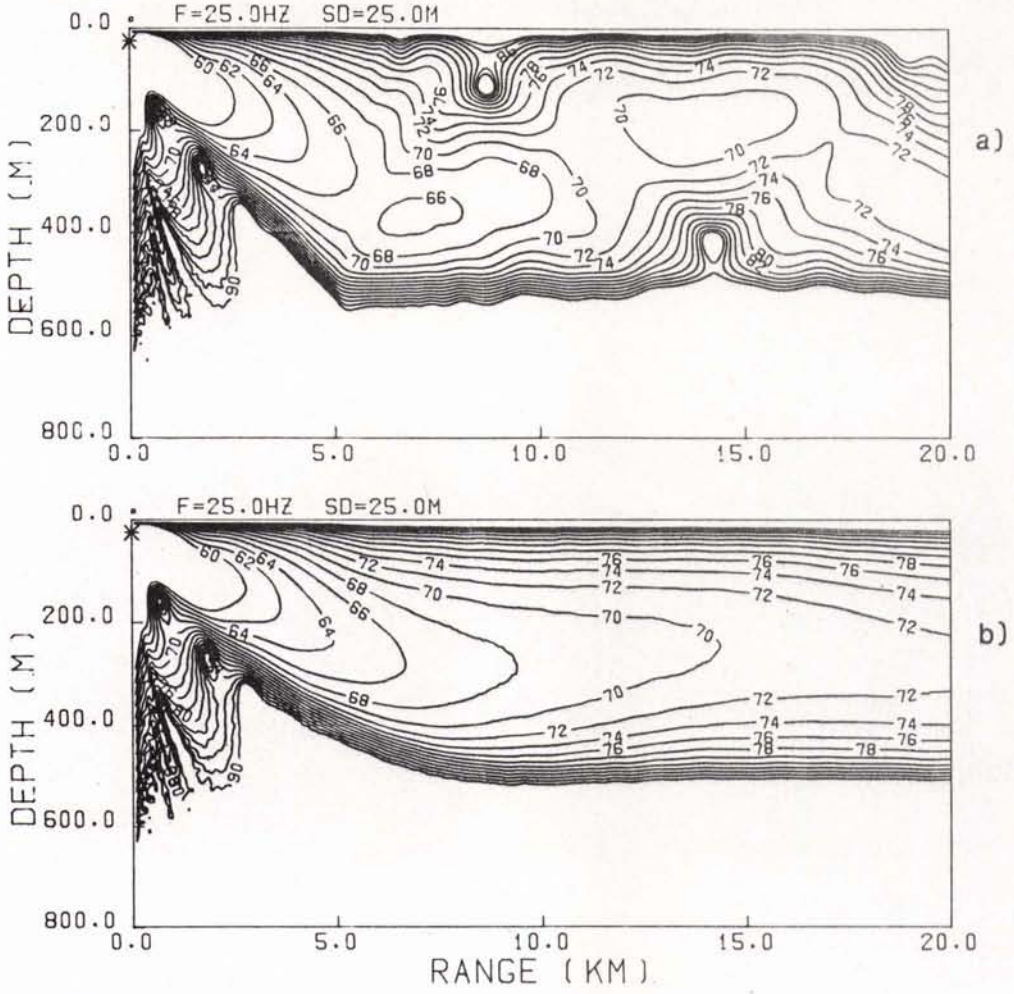

Fig. 20 Down-slope propagation for:
a) a 5° slope followed by a flat bottom, and
b) a smoothly changing bottom slope.

There are several ways to increase the degree of coupling between modes for down-slope situations. Besides the increased coupling with frequency and slope angle, coupling can also be caused by abrupt changes in bottom slope. This is shown in Fig. 20a, which is the same environment as in Fig. 19a, except that the bottom now is flat beyond 5 km. The abrupt change in bottom slope at 5 km results in a complicated contour pattern indicating interference between modes and, hence, the initial first mode has generated (or coupled into) higher modes after the vertex. In this case as many as six modes can exist in the flat part beyond 5 km. That mode coupling is associated with the sharp change of the vertex is shown in Fig. 20b where we gradually go from a 5° slope to a flat bottom. We see that the propagating mode now adapts to the changing water depth exhibiting an "adiabatic" behavior.

6 SUMMARY AND CONCLUSIONS

We have briefly presented an overview over the most commonly used propagation models in underwater acoustics pointed out their areas of applicability, and demonstrated their ability to accurately describe acoustic propagation in complicated ocean environments. It has also been shown that a good agreement between theory and experimental data can be obtained only by including such features as bottom layering, bottom rigidity (shear), scattering at rough boundaries, range-varying environments, etc. Hence the full complexity of a real ocean environment must be considered in the numerical models for accurately predicting the propagation conditions in a given area for a broad range of source frequencies. Finally, the general applicability of the numerical models has been demonstrated by applying the models to some basic wave-propagation problems not tractable by analytical methods.

7 ACKNOWLEDGMENT

This review paper on numerical techniques in underwater acoustics is largely based on material prepared in collaboration with Dr. William A. Kuperman, US Naval Ocean Research and Development Activity, during his 5 years stay at SACLANTCEN.

REFERENCES

1. Officer, C.B. Introduction to the Theory of Sound Transmission. (McGraw-Hill, New York, 1958).
2. Tolstoy, I. and Clay, C.S. Ocean Acoustics: Theory and Experiment in Underwater Sound. (McGraw-Hill, New York, 1966).
3. Tucker, D.G. and Gazey, B.K. Applied Underwater Acoustics. (Pergamon, Oxford, 1966).
4. Tolstoy, I. Wave Propagation. (McGraw-Hill, New York, 1973).
5. Urick, R.J. Principles of Underwater Sound. (McGraw-Hill, New York, 1975).
6. Clay, C.S. and Medwin, H. Acoustical Oceanography. (Wiley, New York, 1977).
7. Keller, J.B. and Papadakis, J.S. (eds.). Wave Propagation and Underwater Acoustics. (Springer-Verlag, Berlin, 1977).
8. De Santo, J.A. (ed.). Ocean Acoustics. (Springer-Verlag, Berlin, 1979).
9. Brekhovskikh, L.M. Waves in Layered Media. (Academic, New York, 1980).
10. Brekhovskikh, L.M. and Lysanov, Yu. Fundamentals of Ocean Acoustics. (Springer-Verlag, Berlin, 1982).

11. DiNapoli, F.R. and Deavenport, R.L. "Theoretical and numerical Green's function field solution in plane multilayered medium", J. Acoust. Soc. Am. 67, 92-105, (1980).
12. Kutschale, H.W. "Rapid computation by wave theory of propagation loss in the Arctic Ocean." Rpt. CU-8-73, Columbia University, Palisades, N.Y. (1973).
13. Schmidt, H. "Modelling of pulse propagation in layered media using a new fast field program." (These proceedings).
14. Ewing, W.M., Jardetzky, W.C. and Press, F. Elastic Waves in Layered Media. (McGraw-Hill, New York, 1957), Chapter 4.
15. Morse, P.M. and Feshbach, H. Methods of Theoretical Physics. (McGraw-Hill, New York, 1953), p. 823.
16. Ingenito, F., Ferris, R., Kuperman, W.A. and Wolf, S.N. "Shallow-water acoustics, summary report, (first phase)". Rpt. 8179, US Naval Research Laboratory, Washington, D.C. (1978).
17. Spofford, C.W. "A synopsis of the AESD workshop on acoustic propagation modelling by non-ray-tracing techniques". Rpt. TN-73-05, Office of Naval Research, Washington, D.C. (1973).
18. Jensen, F.B. and Ferla, M.C. "SNAP: the SACLANTCEN normal-mode acoustic propagation model." Rpt. SM-121, SACLANT ASW Research Centre, La Spezia, Italy (1979).
19. Jensen, F.B. and Kuperman, W.A. "Environmental acoustic modelling at SACLANTCEN". Rpt. SR-34, SACLANT ASW Research Centre, La Spezia, Italy (1979).
20. Ferla, M.C., Jensen, F.B. and Kuperman, W.A. "High-frequency normal-mode calculations in deep water", J. Acoust. Soc. Am. 72, 505-509 (1982).
21. Pierce, A.D. "Extension of the method of normal modes to sound propagation in an almost stratified medium", J. Acoust. Soc. Am. 37, 19-27, (1965).
22. Milder, D.M. "Ray and wave invariants for SOFAR channel propagation", J. Acoust. Soc. Am. 46, 1259-1263 (1969).
23. Williams, A.O. "Normal-mode methods in propagation of underwater sound", in Underwater Acoustics, edited by R.W.B. Stephens (Wiley, London 1970), pp. 23-56.
24. Nagl, A., Uberall, H., Haug, A.J. and Zarur, G.L. "Adiabatic mode theory of underwater sound propagation in range-dependent environment", J. Acoust. Soc. Am. 63, 739-749 (1978).
25. Rutherford, S.R. and Hawker, K.E. "An examination of the influence of range dependence of the ocean bottom on the adiabatic approximation", J. Acoust. Soc. Am. 66, 1145-1151 (1979).
26. Rutherford, S.R. "An examination of multipath processes in a range-dependent ocean environment within the context of adiabatic mode theory", J. Acoust. Soc. Am. 66, 1482-1486 (1979).

27. Chwieroth, F.S., Nagl, A., Uberall, H., Graves, R.D. and Zarur, G.L. "Mode coupling in a sound channel with range-dependent parabolic velocity profile", J. Acoust. Soc. Am. 64, 1105-1112 (1978).
28. Thompson, I.J. "Mixing of normal modes in a range-dependent model ocean", J. Acoust. Soc. Am. 69, 1280-1289 (1981).
29. McDaniel, S.T. "Comparison of coupled-mode theory with the small-waveheight approximation for sea-surface scattering", J. Acoust. Soc. Am. 70, 535-540 (1981).
30. Rutherford, S.R. and Hawker, K.E. "Consistent coupled mode theory of sound propagation for a class of nonseparable problems", J. Acoust. Soc. Am. 70, 554-564 (1981).
31. Evans, R.B. "A coupled mode solution for acoustic propagation in a waveguide with stepwise depth variation of a penetrable bottom," J. Acoust. Soc. Am. 74, 188-195 (1983).
32. Stickler, D.C. "Normal-mode program with both the discrete and branch line contributions", J. Acoust. Soc. Am. 57, 856-861 (1975).
33. Tappert, F.D. "The parabolic approximation method", in Wave Propagation and Underwater Acoustics, edited by J.B. Keller and J.S. Papadakis (Springer-Verlag, Berlin, 1977), pp. 224-287.
34. Jensen, F.B. and Krol, H.R. "The use of the parabolic equation method in sound propagation modelling". Rpt. SM-72, SACLANT ASW Research Centre, La Spezia, Italy, (1975).
35. Davis, J.A., White, D. and Cavanagh, R.C. "NORDA parabolic equation workshop". Rpt. TN-143, Naval Ocean Research and Development Activity, NSTL Station, MS (1982).
36. Lee, D. and Gilbert, K.E. "Recent progress in modeling bottom interacting sound propagation with parabolic equations", in Oceans 82 Conference Record (MTS-IEEE, Washington, D.C., 1982), pp. 172-177.
37. Lee, D., Botseas, G. and Papadakis, J.S. "Finite-difference solution to the parabolic wave equation", J. Acoust. Soc. Am. 70, 795-800 (1981).
38. Lee, D. and Botseas, G. "IFD: an implicit finite-difference computer model for solving the parabolic equation." Rpt. TR-6659, Naval Underwater Systems Center, New London, CT (1982).
39. Jensen, F.B. and Kuperman, W.A. "Consistency tests of acoustic propagation models". Rpt. SM-157, SACLANT ASW Research Centre, La Spezia, Italy (1982).
40. Jensen, F.B. "Sound propagation in shallow water: a detailed description of the acoustic field close to surface and bottom", J. Acoust. Soc. Am. 70, 1397-1406 (1981).
41. Ferla, M.C., Dreini, G., Jensen, F.B. and Kuperman, W.A. "Broadband model/data comparisons for acoustic propagation in coastal waters", in Bottom-Interacting Ocean Acoustics, edited by W.A. Kuperman and F.B. Jensen (Plenum, New York, 1980), pp. 577-592.

42. Jensen, F.B. and Kuperman, W.A. "Optimum frequency of propagation in shallow water environments", J. Acoust. Soc. Am. 73, 813-819 (1983).
43. Jensen, F.B. "Sound propagation over a seamount", in Proceedings of the 11th International Congress on Acoustics, (Paris, 1983).
44. Goos, F. and Hänchen, H. "A new and fundamental experiment on total reflection" (in German), Ann. Phys. (Leipzig) 1, 333-346 (1947).
45. Lotsch, H.K.V. "Beam displacement at total reflection: the Goos-Hänchen effect", Optik (Stuttgart) 32, 116-137 (1970); 32, 189-204 (1970); 32, 299-319 (1971); 32, 553-569 (1971)
46. Tamir, T. and Bertoni, H.L. "Lateral displacement of optical beams at multilayered and periodic structures", J. Opt. Soc. Am. 61, 1397-1413 (1971).
47. Bertoni, H.L. and Tamir, T. "Unified theory of Rayleigh-angle phenomena for acoustic beams at liquid-solid interfaces", Appl. Phys. 2, 157-172 (1973).
48. Shin, S.Y. and Felsen, L.B. "Lateral shifts of totally reflected gaussian beams", Radio Science 12, 551-564 (1977)
49. Ngoc, T.D.K. and Mayer, W.G. "Numerical integration method for reflected beam profiles near Rayleigh angle", J. Acoust. Soc. Am. 67, 1149-1152 (1980).
50. Neubauer, W.G. "Ultrasonic reflection of a bounded beam at Rayleigh and critical angles for a plane liquid-solid interface", J. Appl. Phys. 44, 48-55 (1973).
51. Breazeale, M.A., Adler, L. and Scott, G.W. "Interaction of ultrasonic waves incident at the Rayleigh angle onto a liquid-solid interface", J. Appl. Phys. 48, 530-537 (1977).
52. Pitts, L.E., Plona, T.J., and Mayer, W.G. "Theory of nonspecular reflection effects for an ultrasonic beam incident on a solid plate in a liquid", IEEE Trans. Sonics Ultrasonics SU-24, 101-109 (1977).
53. Claeys, J.M. and Leroy, O. "Reflection and transmission of bounded beams on half-spaces and through plates", J. Acoust. Soc. Am. 72, 585-590 (1982).
54. Muir, T.G., Horton, C.W. and Thompson, L.A. "The penetration of highly directional acoustic beams into sediments", J. Sound Vibr. 64, 539-551, (1979).
55. Tjøtta, J.N. and Tjøtta, S. "Theoretical study of the penetration of highly directional acoustic beams into sediments, J. Acoust. Soc. Am. 69, 998-1008 (1981).
56. Coppens, A.B. and Sanders, J.V. "Propagation of sound from a fluid wedge into a fast fluid bottom", in Bottom-Interacting Ocean Acoustics, edited by W.A. Kuperman and F.B. Jensen (Plenum Press, New York, 1980), pp. 439-450.
57. Jensen, F.B. and Kuperman, W.A. "Sound propagation in a wedge-shaped ocean with a penetrable bottom", J. Acoust. Soc. Am. 67, 1564-1566 (1980).

58. Pierce, A.D. "Guided mode disappearance during upslope propagation in variable depth shallow water overlying a fluid bottom", J. Acoust. Soc. Am. 72, 523-531 (1982).
59. Arnold, J.M. and Felsen, L.B. "Rays and local modes in a wedge-shaped ocean", J. Acoust. Soc. Am. 73, 1105-1119 (1983).
60. Kamel, A. and Felsen, L.B. "Spectral theory of sound propagation in an ocean channel with weakly sloping bottom", J. Acoust. Soc. Am. 73, 1120-1130 (1983).

MODELLING OF PULSE PROPAGATION IN LAYERED MEDIA USING A NEW FAST FIELD PROGRAM

Henrik Schmidt

SACLANT ASW Research Centre
Viale San Bartolomeo 400
19026 La Spezia, Italy

ABSTRACT

Numerical modelling of acoustic pulse propagation in stratified solid media is often found to be impractical due to the comprehensive calculations involved. Here a new numerical model, of the fast field type, is presented. Instead, of using the Thomson-Haskell matrix method, as done in earlier models of the same type, the depth-separated wave equation is solved by a numerical technique very similar to that used in finite element programs. The speed improvement has been considerable, especially in cases with many sources and receivers. The model has been implemented on an FPS164 array processor and used for analysis of seismic pulse propagation in a shallow water environment and reflection of pulsed ultrasonic beams from a fluid-solid interface.

INTRODUCTION

A number of numerical models are available for investigating sound propagation in layered media. Each model is based on a set of assumptions and approximations and dedicated to specific applications. In relation to underwater acoustics four types of models are of interest, known as ray, normal-mode, parabolic equation, and fast field models. Jensen <1> has reviewed and classified these models and here we will concentrate on models of the last type, the fast field programs (FFP).

These models yield an exact solution to the depth-separated wave equation for horizontally stratified environments. Depending

on the geometry (plane or cylindrical) the field is decomposed into plane or conical waves. The field corresponding to each horizontal wavenumber is then found by matching of boundary conditions at each interface, and the total field is found by superposition. In the case of cylindrical geometry the superposition is given by a Hankel transform integral. By replacing the Hankel function with its large argument approximation, this is changed to a Fourier integral, which after truncation can be evaluated by means of a fast Fourier technique. This approximation of the Hankel transform was originally introduced by Marsh <2> and is usually called the fast field technique.

The major part of the numerical effort is related to the solution of the depth-separated wave equation. DiNapoli <3> introduced an FFP-code that performed the solution very efficiently by means of recurrence relations for the hypergeometric functions. However, his approach allows only for fluid layers, and in such cases other models will often be more convenient, e.g. normal-mode models.

The main advantage of FFP-models are their ability to treat problems involving solid layers <1>. The first model to include this feature was introduced by Kutschale <4>. As shear properties are very important for sound propagation in shallow water <5>, this model has been used extensively for such problems during the last decade. Kutschale solved the depth-separated wave equation using a Green's-function approach based on the Thomson-Haskell matrix method. However, this method allows for only one source and receiver at a time, and even in such cases the computations are rather extensive, often the modelling of pulse propagation becomes impractical since this has to be carried out by means of Fourier synthesis involving many frequency components.

Here a new FFP-code, called SAFARI, is introduced. Instead of using the Thomson-Haskell method, a system of linear equations in the unknown potentials is set up and solved at each horizontal wavenumber. When the layer series is given, it is possible from the boundary conditions to determine a priori a mapping between the equations to be satisfied at each interface and a global set of equations. A significant number of wavenumber-independent expressions can then be evaluated once. The mapping technique is very similar to the one used in finite-element programs.

The source contributions are mapped into the righthand side of the global equations, and there is no theoretical limit for the number of sources.

The receiver depth is not included in the system of equations, and any number of receivers can therefore be treated with only one solution.

Even with one source/receiver combination, the calculation speed has been improved by up to one order of magnitude. This gain in speed and performance has made the FFP-technique a more realistic alternative to other numerical techniques, and in areas where this technique is the only possibility, the range of solvable problems has been increased considerably.

In the following the model and its mathematical background is described, and two examples of its use are given. First it is used to clarify some of the basic properties of the slow seismic interface waves that can be observed in shallow water environments. Synthetic seismograms are produced and compared qualitatively to experimental data. Then the model is used to determine the reflection of a pulsed beam from a water/aluminium-oxide interface.

1 THE MATHEMATICAL MODEL

The mathematical model is based on the assumption that the water column and the bottom consist of a series of range-independent layers. All materials are considered to be homogeneous and isotropic elastic continua with Lamé constants λ_n and μ_n and density ρ_n. The subscript refers to layer number n. The damping mechanisms are assumed to be linear viscoelastic.

A cylindrical coordinate system $\{r,\theta,z\}$ is introduced with the z-axis going through the source and being positive downwards (Fig. 1). The representation of the cylindrical displacement components $\{u,v,w\}$ in terms of scalar potentials and the subsequent expression of these as Hankel transforms closely follows the presentation given by Schmidt and Krenk <6>; hence, only an outline will be given here. If body forces are neglected, the displacement equation of motion will be satisfied if the displacement components in layer n are expressed in terms of three scalar potentials $\{\Phi_n,\Psi_n,\Lambda_n\}$ as

$$
\begin{aligned}
u\,|_n &= \frac{\partial \Phi_n}{\partial r} + \frac{1}{r}\frac{\partial \Psi_n}{\partial \theta} + \frac{\partial^2 \Lambda_n}{\partial r \partial z} \\
v\,|_n &= \frac{1}{r}\frac{\partial \Phi_n}{\partial \theta} - \frac{\partial \Psi_n}{\partial r} + \frac{1}{r}\frac{\partial^2 \Lambda_n}{\partial \theta \partial z} \qquad (1) \\
w\,|_n &= \frac{\partial \phi_n}{\partial z} - \left(\frac{1}{r}\frac{\delta}{\partial r}\, r\, \frac{\delta}{\partial r} + \frac{1}{r^2}\frac{\partial^2}{\partial \theta^2}\right) \Lambda_n \ ,
\end{aligned}
$$

where the potentials satisfy the wave equations:

$$\left(\nabla^2 - \frac{1}{C_{Ln}^2}\frac{\partial^2}{\partial t^2}\right)\Phi_n = 0 \qquad (2)$$

$$\left(\nabla^2 - \frac{1}{C_{Tn}^2}\frac{\partial^2}{\partial t^2}\right)(\Psi_n, \Lambda_n) = 0, \qquad (3)$$

in which C_L and C_T are the velocities of the compressional and shear waves, respectively:

$$C_{Ln}^2 = \frac{\lambda_n + 2\mu_n}{\rho_n} \qquad (4)$$

$$C_{Tn}^2 = \frac{\mu_n}{\rho_n} \; . \qquad (5)$$

In the present case the field is asymmetric due to the positioning of the source on the axis, and the angular displacement v vanishes everywhere. It is then clear from Eq. 1 that the potential Ψ_n must be constant and can be excluded.

In the following, only vibrations with angular frequency ω will be considered; displacements, stresses and potentials can then be expressed in complex form with the common factor $\exp(i\omega t)$. This factor will not be included in the following. The viscoelastic damping can now be accounted for by allowing the Lamé constant to be complex. After use of the Hankel transform on the wave equations, the following integral representations are obtained for the potentials:

$$\Phi_n(r,z) = \int_0^\infty \left\{A_n^-(s)e^{-z\alpha_n(s)} + A_n^+(s)e^{z\alpha_n(s)}\right\} J_o(rs)s\, ds \qquad (6)$$

$$\Lambda_n(r,z) = \int_0^\infty \left\{B_n^-(s)e^{-z\beta_n(s)} + B_n^+(s)e^{z\beta_n(s)}\right\} J_o(rs)s\, ds, \qquad (7)$$

where

J_m is the Bessel function of the first kind and order m,

A_n^-, A_n^+, B_n^- and B_n^+ are arbitrary functions in the horizontal wavenumber S.

$\alpha_n(s)$, $\beta_n(s)$ are defined as

$$\alpha_n(s) = \begin{cases} \sqrt{(s^2-h_n^2)}, & s > \mathrm{Re}\{h_n\} \\ i\sqrt{(h_n^2-s^2)}, & s < \mathrm{Re}\{h_n\} \end{cases} \tag{8}$$

$$\beta_n(s) = \begin{cases} \sqrt{(s^2-k_n^2)}, & s > \mathrm{Re}\{k_n\} \\ i\sqrt{(k_n^2-s^2)}, & s < \mathrm{Re}\{k_n\}. \end{cases} \tag{9}$$

The wavenumbers h_n and k_n for the compressional and shear waves, respectively, are defined by

$$h_n^2 = \left(\frac{\omega}{C_{Ln}}\right)^2 = \frac{\omega^2\rho_n}{\lambda_n+2\mu_n} \tag{10}$$

$$k_n^2 = \left(\frac{\omega}{C_{Tn}}\right)^2 = \frac{\omega^2\rho_n}{\mu_n} \tag{11}$$

If Eqs. 6 and 7 are inserted into Eq. 1, the following expressions are obtained for the particle displacements:

$$w(r,z)\Big|_n = \int_0^\infty \{-\alpha_n A_n^- e^{-z\alpha_n} + \alpha_n A_n^+ e^{z\alpha_n} + sB_n^- e^{-z\beta_n} + s B_n^+ e^{z\beta_n}\} s J_0(rs)ds, \tag{12}$$

$$u(r,z)\Big|_n = \int_0^\infty \{-s A_n^- e^{-z\alpha_n} - s A_n^+ e^{z\alpha_n} + \beta_n B_n^- e^{-z\beta_n} - \beta_n B_n^+ e^{z\beta_n}\} s J_1(rs)ds. \tag{13}$$

The stress components involved in the boundary conditions follow from Hooke's law:

$$\sigma_{zz}(r,z)\Big|_n = \mu_n \int_0^\infty \{(2s^2-k^2)(A_n^- e^{-z\alpha_n} + A_n^+ e^{z\alpha_n}) + 2s\beta_n(-B_n^- e^{-z\beta_n} + B_n^+ e^{z\beta_n})\} s J_0(rs)ds, \tag{14}$$

$$\sigma_{rz}(r,z)\Big|_n = \mu_n \int_0^\infty \{2s\alpha_n(A_n^- e^{-z\alpha_n} - A_n^+ e^{z\alpha_n}) - (2s^2-k^2)(B_n^- e^{-z\beta_n} + B_n^+ e^{z\beta_n})\}\, s\, J_1(rs)\, ds. \quad (15)$$

In the case of a fluid layer the shear stiffness μ_n vanishes, and only the potential Φ_n is involved. The displacements follow directly from Eqs. 12 and 13 by setting B^- and B^+ to zero. The shear stress is identically zero, whereas Eq. 14 has to be replaced by

$$\sigma_{zz}(r,z)\Big|_n = -\lambda_n h^2 \int_0^\infty \{A_n^- e^{-z\alpha_n} + A_n^+ e^{z\alpha_n}\}\, s\, J_0(rs)ds. \quad (16)$$

The source is assumed to be in layer number m at depth z_s. In the absence of boundaries, the field produced in layer m would be <7>:

$$\Phi_s(r,z) = \frac{iS_\omega}{4\pi} \int_0^\infty \frac{e^{-|z-z_s|\alpha_m}}{\alpha_m}\, s\, J_0(rs)ds\ , \quad (17)$$

$$\Lambda_s(r,z) \equiv 0\ , \quad (18)$$

where S_ω is the source strength. If Eq. 17 is inserted into Eq. 1, expressions similar to Eqs. 12 and 13 are obtained for the displacements, and again Hooke's law yields expressions like Eqs. 14 and 15 for the stresses involved in the boundary conditions.

For each value of the range, r, the boundary conditions must be satisfied. In the upper and lower half-spaces the arbitrary functions, with superscript - and + respectively, must vanish due to the radiation condition. At each interface, w and σ_{zz} must be continuous, and at all solid/liquid interfaces the shear stresses must vanish. At solid/solid interfaces, w, u, σ_{zz} and σ_{rz} must be continuous. This yields a linear system of equations in the arbitrary functions, to be satisfied at each horizontal wavenumber:

$$C_{ij}(s) \cdot A_j(s) = R_i(s). \quad (19)$$

The vector $A_j(s)$ contains all the non-vanishing arbitrary functions, $C_{ij}(s)$ is the coefficient matrix, and $R_i(s)$ contains the contributions from the source. When the arbitrary functions are found, the field parameters at any depth and range can be obtained from the Hankel transforms (Eqs. 12 to 16) plus the source contributions (if the source and receiver are in the same layer).

An analytical solution of Eq. 19 is of course possible, leading to closed-form expressions for the arbitrary functions; but for more than a few layers this procedure would be inconvenient. Further, the Hankel transforms do not lead to closed-form solutions, but need numerical evaluation. Thus the most general way to proceed is to create a numerical model based directly on the system of equations (Eq. 19). Such a model is described in the next chapter.

2 THE NUMERICAL MODEL SAFARI

The numerical evaluation of the Hankel transform necessitates a truncation and a discretization in the horizontal wavenumber s. As can be observed from Eqs. 8 and 17, the source terms decay exponentially for s going towards infinity. As the source terms form the righthand side of Eq. 19 the arbitrary functions will behave in the same way. It is therefore possible to truncate the integration interval in accordance with any accuracy demands. The fast-field technique introduced by Marsh <7> can then be used to evaluate the Hankel transforms.

The Bessel functions are expressed in terms of Hankel functions

$$J_m(rs) = 1/2 \left[H_m^{(1)}(rs) + H_m^{(2)}(rs) \right] \tag{20}$$

and each integral is split into two. As only outgoing waves are considered, the integrals involving $H_m^{(1)}(rs)$ are neglected, and $H_m^{(2)}(rs)$ is replaced by its asymptotic form

$$H_m^{(2)}(rs) \underset{rs\to\infty}{\sim} \sqrt{\left(\frac{2}{\pi rs}\right)}\, e^{-i\left[rs-\left(m+\frac{1}{2}\right)\frac{\pi}{2}\right]} \tag{21}$$

The integration over the truncated interval can now be performed by means of the fast Fourier transform, and the actual field parameter is found at a number of ranges equal to the number of discrete wavenumbers considered.

DiNapoli and Deavenport <3> have compared Marsh's method to the technique introduced by Tsang, Brown, Kiang and Simmons <8>, which does not use the asymptotic form of the Hankel function. Significant differences were found only for very short ranges.

The kernels in the Hankel transforms are now needed only for a limited number of discrete values of s. Kutschale <4> used a Green's-function approach based on the Thomson-Haskell matrix

method. However, his approach allows for only one source/receiver combination at a time.

In the SAFARI model Eq. 19 is set up and solved directly. When the layer series is given, it is possible to determine a priori a mapping between the equations to be satisfied at each interface and the global system of equations, Eq. 19. The unknown arbitrary functions are mapped into the vector A_j, the coefficients into the matrix C_{ij}, and the source contributions into the right side R_j of Eq. 19. If more than one source is present, the contributions are simply added.

The receiver depth is not included in Eq. 19, thus yielding the possibility of determining the field at any depth from Eqs. 12 to 16 with only one solution of Eq. 19.

The mapping between the local and the global system of equations is very similar to the technique used in finite element programs. By using this technique the computer code can become very efficient since a significant number of calculations can be done only once. Furthermore, the code will be straightforward to vectorize, thus making it well suited for implementation on an array processor.

The solution of Eq. 19 is performed by means of gaussian elimination with partial pivoting.

In cases with only one source/receiver combination, SAFARI is found to be an order of magnitude faster than Kutschale's model. In cases with several sources or receivers the speed gain is of course much bigger.

This surprisingly high speed gain is believed to be due to the mapping technique, which partly ensures that a large amount of unnecessary calculation is avoided, and partly makes efficient programming possible.

The implementation of SAFARI on an FPS164 attached processor has given at least one order of magnitude further, and a number of problems, which were impractical to treat numerically, can now be solved with an acceptable amount of computation time. A couple of examples are given in the following.

3 MODELLING OF SEISMIC INTERFACE WAVES

The importance of the shear properties of the sea-bed for acoustic wave propagation in shallow water is well established <5>. Unfortunately the shear parameters are very difficult to isolate experimentally. The shear parameters are, however, indirectly pre-

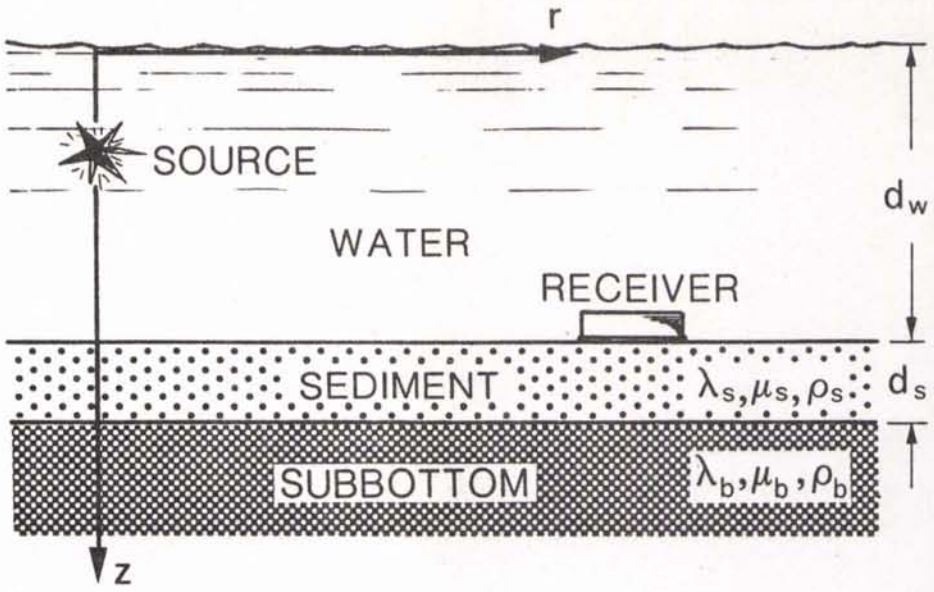

Fig. 1 Stratified shallow water environment

sent through the properties of the measurable seismic interface waves, and much effort has been put into an experimental investigation of these <9>, <10>.

Since no applicable inverse models are available the shear properties are determined by "trial-and-error" — methods using numerical propagation models <10>, <11>. Usually several parameters are unknown and, since the calculations needed for each combination are rather comprehensive, the determination of the shear parameters in this way can become very expensive in terms of calculation time. It is therefore important a priori to be able to determine approximate values directly from the experimental data.

With this in view, the SAFARI model has been used to clarify some of the propagation characteristics of the seismic interface waves for different shallow water environments. A detailed description of the investigation is given in <12>, and only a couple of examples will be given here.

In order not to obscure the basic principles, a simple 2-layered model was chosen for the sea-bed, Fig. 1. Below the water column of depth d_w, a single sediment layer of thickness d_s covers a half-space of rock or rock-like material. The bottom materials used in the examples and their assumed properties are listed in Table 1. The complex Lamé constants are not given explicitly in the table. Instead the compressional and shear velocities are shown, together with their respective dampings in dB per wavelength.

TABLE 1

MATERIAL PROPERTIES

Material	Density ρ(g/cm^3)	Compressional Speed C_L(m/s)	Shear Speed C_T(m/s)	Compressional attenuation γ_L(dB/λ)	Shear attenuation γ_T(dB/λ)
Water	1.0	1500	-	-	-
Silt	1.8	1600	200	1.0	2.0
Sand	2.0	1800	600	0.7	1.5
Limestone	2.2	2250	1000	0.4	1.0
Basalt	2.6	5250	2500	0.2	0.5

The water depth is chosen to be 100 m, and a silt layer of 50 m thickness is combined with either a limestone or a basalt sub-bottom.

A point source is placed in the middle of the water column at 50 m depth, and the vertical particle velocity at the top of the sediment layer is calculated using a pressure amplitude of 1 Pa at a distance of 1 m from the source. Only frequencies below and around the cut-off frequency for the first water mode are considered, which in the present case means frequencies below 10 Hz. In the first test case a 50 m silt sediment layer covers a limestone sub-bottom. Figure 2 shows the modulus of the integrand in the Hankel transform of the vertical velocity at the top of the sediment layer for a frequency of 1.5 Hz. No water modes are present at this frequency, but two mode-like peaks can be observed at wavenumbers corresponding to phase velocities of 300 m/s (peak '1') and 840m/s (peak '2'). These peaks correspond to interface waves, and will be denoted the first and second interface mode, respectively. The first interface mode is best excited (highest amplitude), but it also has the highest damping (widest peak).

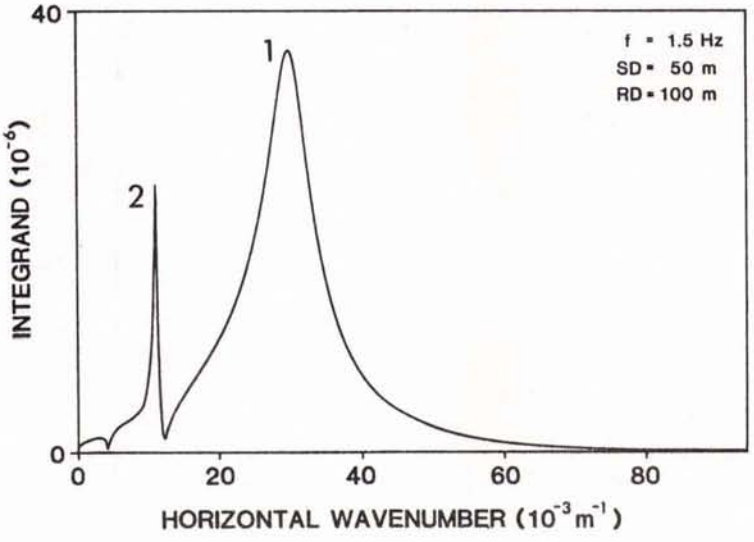

Fig. 2 Hankel transform of vertical particle velocity at 1.5 Hz. 50 m silt on limestone.

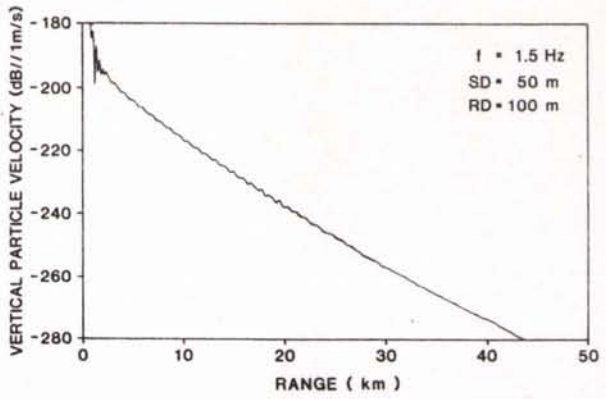

Fig. 3 Vertical particle velocity as function of range at 1.5 Hz. 50 m silt on limestone.

Figure 3 shows the corresponding vertical particle velocities at ranges up to 50 km. Due to the high damping of the first interface mode, its contribution is significant only for ranges shorter than 2 km, beyond which the second interface mode becomes dominant.

If the source is not of stationary type, but transient, the different velocities of the two interface modes will yield different arrival times, and the presence of the first interface mode will be measurable also at larger ranges. The phase and group velocities of the two interface modes have been calculated in the frequency band of interest, 0.1 to 10 Hz, with a resolution of 0.1 Hz. The results are shown in Fig. 4 together with an excitation measure, which somewhat arbitrarily has been chosen to be the particle velocity at 10 km range.

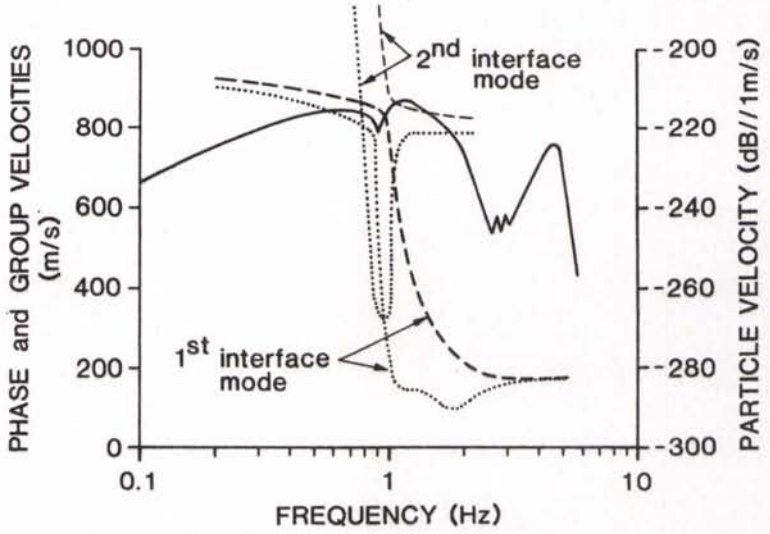

Fig. 4 Excitation and dispersion curves. 50 m silt on limestone.

There is only one interface mode at frequencies below 1 Hz. It is slightly dispersive, with phase and group velocities approaching those of a Rayleigh wave on a limestone half-space. At 1 Hz a very sharp transition zone appears, where the velocities drop dramatically to values approaching those of a Scholte wave at a water/silt interface. At 1.8 Hz the group velocity reaches a minimum of 100 m/s, i.e. half the shear speed in silt. The second interface mode has a sharp cut-off at the transition frequency, and after a distinct minimum of the group velocity it appears as a logical continuation of the low-frequency part of the first interface mode. Above 2 Hz the excitation (solid line) of the second interface mode decreases due to the increased distance in terms of wavelengths of the source from the silt/limestone interface, along which the second interface mode propagates. The sharp peak on the excitation curve around 4.5 Hz is the first propagating water mode.

The existence of mode transition zones is well known from the theory of vibration of elastic plates, Mindlin <13>, where they appear near the thickness-shear frequencies. These are the frequencies at which an infinite elastic plate can perform free shear vibrations with vanishing vertical displacements. Now consider the silt layer as an infinite elastic plate in welded contact with an infinite rigid half-space. The first thickness-shear frequency would then correspond to that of a free silt plate of the double thickness, Mindlin <13>:

$$f_{TS} = \frac{C_T}{4d_S} \tag{22}$$

where C_T is the shear velocity and d_S is the thickness of the layer. If the parameters for silt are applied to Eq. 22, we obtain f_{TS} equal to 1 Hz, which is very close to the observed transition frequency in Fig. 4.

Since the transition frequency can be observed in experimental results, its correlation with the thickness-shear frequency could yield a direct method of determining the shear-wave velocity in a single sediment layer overlying a rigid half-space.

To summarize the general propagation characteristics for this test case (Fig. 4), the computed particle velocity at 10 km range is entirely associated with the first interface mode below the transition frequency (1 Hz). This interface mode is strongly related to a Rayleigh wave on a limestone half-space below 1 Hz, while it becomes an interface wave connected with the water/silt interface at frequencies above 1 Hz. In this frequency regime the second interface mode appears, and it is mainly related to the silt/limestone interface. Finally, the first water-borne mode appears at around 4.5 Hz.

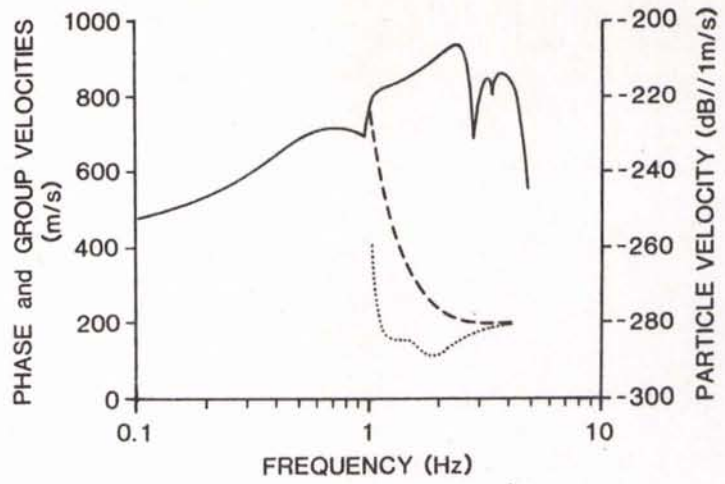

Fig. 5 Excitation and dispersion curves. 50 m silt on basalt.

A silt layer on basalt was also studied in order to analyze the effect of different sub-bottom materials. In this case (Fig. 5) the low-frequency part of the first interface mode is excited only slightly, but the transition zone can again be observed near the thickness-shear frequency of 1 Hz. Above 1 Hz the dispersion curves are very similar to those obtained earlier for a sub-bottom of limestone (Fig. 4).

Synthetic seismograms have been produced for the two test cases in order to illustrate the time-domain effect of the features described above. The source is assumed to be half a sine wave of 1.5 Hz sent through an ideal 0.5 to 3.2 Hz band-pass filter. This frequency range has been chosen as it contains frequencies on both sides of the transition frequency for a silt-sediment layer of 50 m thickness. The transfer functions were calculated to a resolution of 0.01 Hz and multiplied by the spectrum of the source. The time series were then created by means of the fast-Fourier transform at ranges of 1, 2, 3, 4 and 5 km.

Figure 6 shows the result for test case 1, i.e. a 50 m silt layer on a limestone half-space. The first weak arrival corresponds to a compressional wave in the limestone, whereas the first significant arrival corresponds to the Rayleigh wave velocity of the limestone (900 m/s). This arrival consists of the low-frequency parts of the first and second interface modes. A clear dispersion can be observed corresponding to the distinct minimum in the group velocity of the second interface mode in Fig. 4. The slow highly damped wave corresponding to the first interface mode above the transition frequency propagates with group velocities between 100 and 180 m/s, again in good agreement with Fig. 4. At ranges greater than 4 km this arrival has negligible amplitude.

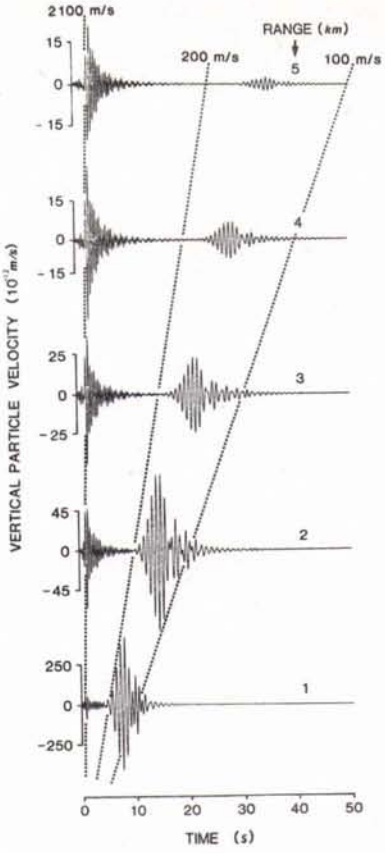

Fig. 6
Stacked synthetic seismograms.
50 m silt on limestone.

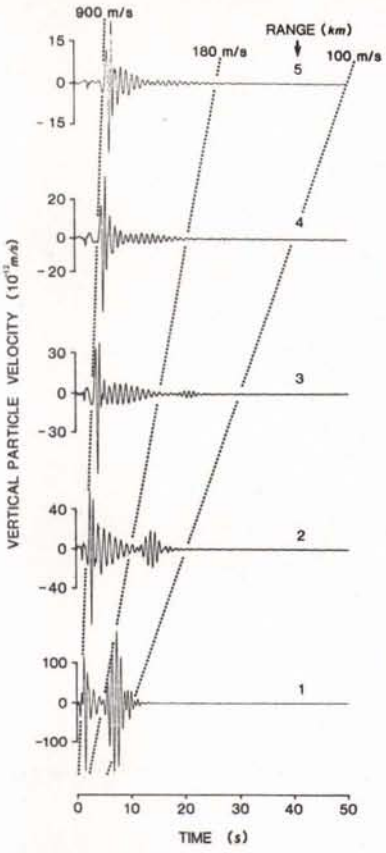

Fig. 7
Stacked synthetic seismograms.
50 m silt on basalt.

As described above, the low-frequency part of the first interface mode will not be significantly excited if the sub-bottom is basalt. The maximum excitation at 10 km range lies at 2.5 Hz (Fig. 5) and is due to a strong excitation of the second mode. These properties are also reflected in the synthetic seismograms (Fig. 7). The fastest arrival, apart from the weak compressional wave, has its major frequency content above 2 Hz and corresponds mainly to the high-frequency end of the second interface mode. The severe dispersion of the corresponding arrival in Fig. 6 is not present here, and the slow part of the first interface mode is well separated, travelling at group velocities between 100 and 200 m/s. The synthetic seismograms in Figs. 6 and 7 are, at least qualitatively, very similar to those observed during experiments, Fig. 8 <15>.

With 4096 sample points in the wavenumber space the calculation time on an FPS164 array processor, was 9 secnds for each frequency or 40 minutes in total for the synthetic seismograms in Figs. 6 or 7.

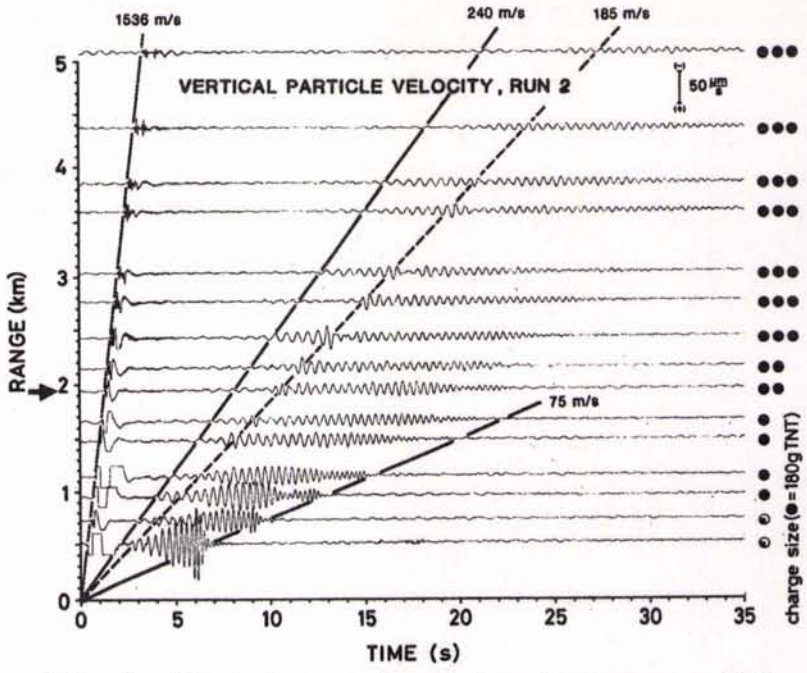

Fig. 8 Stacked experimental seismograms, <15>.

4 REFLECTION OF A PULSED BEAM AT A FLUID/SOLID INTERFACE

As mentioned above, the solution technique used in SAFARI yields the possibility of treating problems in which many sources and receivers are involved.

Jensen <1>, used the model to treat the problem of reflection of narrow ultrasonic beams at a water/aluminium-oxide interface at grazing angles near the Rayleigh angle, i.e. the angle where a leaky interface wave is excited. A monochromatic analysis was performed in order to clarify the influence of beam divergence on the reflection pattern, and excellent agreement was obtained with both experimental and theoretical results reported in the literature. In addition, some apparent discrepancies between experimental and theoretical results were resolved.

One of the results from <1> is shown in Fig. 9. A parallel gaussian beam is generated by a linear vertical source-array of 649 elements, spaced half a wavelength apart. The mid-point of the array is placed 40 cm above the interface, the frequency is 2 MHz, and the grazing angle of the beam is 75.2°, corresponding to the Rayleigh angle for water/aluminium-oxide. The splitting of the reflected beam is easily observed. The specularly reflected beam and the beam caused by the leaky interface wave are separated by a strip of low intensity.

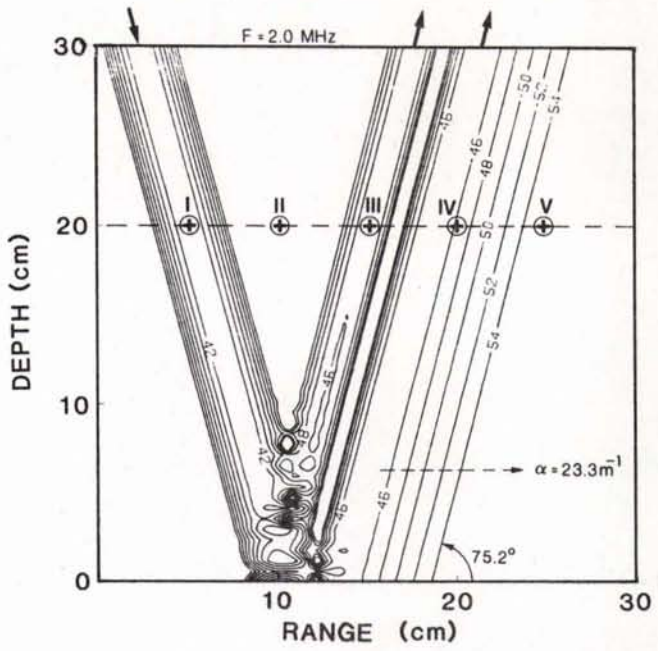

Fig. 9
Reflection of a 2 MHz beam from a water/aluminum-oxide interface at the Rayleigh angle.

As pointed out by Bertoni and Tamir <14> this zero-strip is due to destructive interference between the two parts of the reflected field. If the surfaces of equal phase are plane and perpendicular to the direction of propagation, which is the case for parallel beams, the two reflected beams thus have to be 180° out of phase.

This feature can of course be demonstrated by making a cut perpendicular to the propagation direction, but if the continuous beam is replaced by a pulsed beam, the phase shift will yield an amplitude inversion of the pulse in the two beams, independent of the position of the receivers within the beams. Furthermore, a pulse calculation will yield information on arrival times for the pulse at different receivers.

To demonstrate this the pulse version of SAFARI was used to calculate the received signals at five different receivers, all situated 20 cm above the interface as indicated in Fig. 9.

As pulse calculations in SAFARI are performed by means of discrete Fourier synthesis, it is very important to choose the time window correctly in order to avoid time-domain aliasing.

The approximate arrival times were therefore determined using a narrow-banded source pulse (1.8 to 2.2 MHz). The time window was chosen to be 0 to 1 ms, yielding frequency steps of 1 kHz. The calculated time series for the five receivers are shown in Fig. 10. The vertical scale is arbitrary, but is the same for all five receivers.

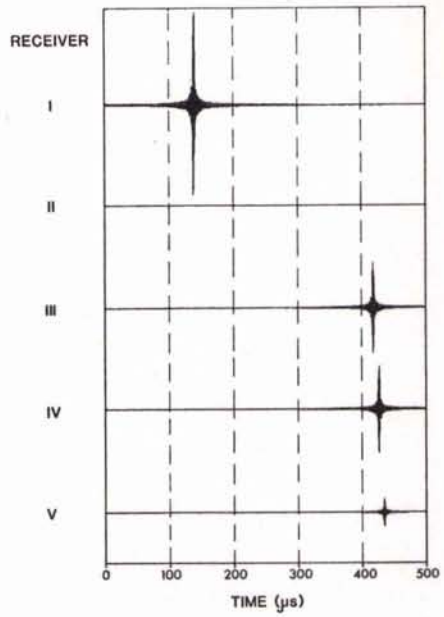

Fig. 10
Received narrow-band pulses at receivers I-V.

The pulse arrives at the reference receiver (I) at t ~ 140 μs. As could be expected from Fig. 9, no significant arrivals appear at receiver II, whereas the reflected pulses arrive at the three last receivers at times between 410 and 440 μs approximately.

A closer analysis is now possible using time windows of 125 μs width. In order to obtain short pulses, the bandwidth is increased to 1.5 MHz to 3.0 MHz. The results are shown for receiver I, III and IV in Fig. 11. The time scale shows the time relative to the expected arrival times. These are determined by geometrical means. A plane wave of grazing angle 75.2° that passes the reference receiver I at t = 139.30 μs will be reflected and pass receiver III at t = 416.00 μs. The calculated pulse at this receiver is seen to correspond exactly to this behaviour; the specularly reflected beam has no phase shift. The loss in amplitude is due to the fact that some of the energy is transferred into the leaky Rayleigh wave. The expected arrival at receiver IV is determined in a slightly different way. A ray at a grazing angle of 75.2° is assumed to pass the reference receiver at t = 139.30 μs. When it reaches the interface it travels at the speed of the Rayleigh wave (5825.55 m/s) along the interface, and finally it travels upwards at angle of 75.2° to receiver IV. The arrival time determined by these assumptions is 424.60 μs, again in excellent agreement with the numerical result in Fig. 11. The 180° phase shift is easily observed, thus verifying the explanation for the zero-strip given in <14>.

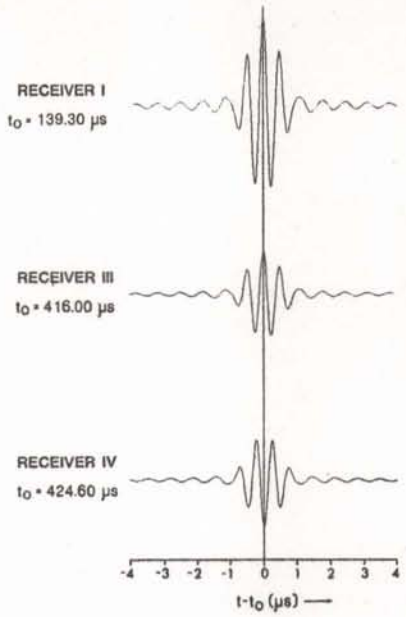

Fig. 11 Arrival of broad-band pulses at receivers I, III and IV related to expected arrival time t_o.

With 512 sampling points in the wavenumber space, the calculation time on the FPS164 was 8 seconds for each frequency, in total 40 minutes for Figs. 10 and 25 minutes for Fig. 11.

CONCLUSIONS

A new fast field program, SAFARI, has been developed. The program is meant for modelling sound and stress wave propagation in horizontally stratified fluid and solid media. By introducing a more efficient solution technique, the computational speed has been improved by an order of magnitude, in some cases even more, compared with earlier models of the same type. Furthermore, the SAFARI model is capable of treating several sources and receivers with only one solution of the wave equation, thus making it feasible to treat problems, in which the field is generated by vertical source arrays.

The model is basically monochromatic, but the increase in speed, together with the fact that the model is well suited for implementation on an array processor, has yielded the possibility of treating pulse propagation by means of Fourier synthesis with limited demands on computation time. This has been demonstrated by a couple of examples, but the range of problems that could be treated is of course much wider.

REFERENCES

1. Jensen, F.B. Numerical models in underwater acoustics (These proceedings).
2. Marsh, H.W., Schulkin, M. and Kneale, S.G. Scattering of underwater sound by a sea surface. Jnl Acoustical Society of America 33, 1961: 334-340.
3. DiNapoli, F.R. and Deavenport, R.L. Theoretical and numerical Green's function field solution in a plane multilayered medium. Jnl Acoustical Society of America 67, 1980: 92-105.
4. Kutschale, H.W. Rapid computations by wave theory of propagation loss in the Arctic Ocean, Rpt CU-8-73. Palisades, NY, Columbia University, 1973.
5. Akal, T. and Jensen, F.B. Effects of the sea-bed on acoustic propagation. In: PACE, N.G. ed. Acoustics and the Sea Bed, Proceedings of an Institute of Acoustics Underwater Acoustics Group Conference, Bath, U.K., University Press, 1983: pp 225-232.
6. Schmidt, H. and Krenk, S. Asymmetric vibrations of a circular plate on an elastic half-space. International Journal of Solids and Structures 18, 1982: 91-105.
7. Ewing, W.M., Jardetzky, W.C. and Press, F. Elastic Waves in Layered Media. New York, NY, McGraw-Hill, 1957.
8. Tsang, L., Brown, R., Kong, J.A., and Simmons, G. Numerical evaluation of electromagnetic fields due to dipole antennas in the presence of stratified media. Jnl Geophysical Research 79, 1974: 2077-2080.
9. Rauch, D. and Schmalfeldt, B. Ocean-bottom interface waves of the Stoneley/Scholte type: properties, observations and possible use. In: PACE, N.G. ed. Acoustics and the Sea Bed, Proceedings of an Institute of Acoustics Underwater Acoustics Group Conference, Bath, U.K., University Press, 1983: pp 307-316.
10. Holt, R.M., Hovem, J.M. and Syrstad, V. Shear modulus profiling of near-bottom sediments using boundary waves. In: PACE, N.G. ed. Acoustics and the Sea Bed, Proceedings of an Institute of Acoustics Underwater Acoustics Group Conference, Bath, U.K., University Press, 1983: 317-325.
11. Essen, H.-H. Model computations for low-frequency surface waves on marine sediments. In: KUPERMAN, W.A. and JENSEN, F.B. eds. Bottom-interacting Ocean Acoustics. Proceedings of a conference held at SACLANTCEN, La Spezia, Italy, 9-12 June 1980. New York, NY, Plenum, 1980: pp 113-118.
12. Schmidt, H. Excitation and propagation of interface waves in a stratified sea-bed. In: PACE, N.G. ed. Acoustics and the Sea Bed, Proceedings of an Institute of Acoustics Underwater Acoustics Group Conference, Bath, U.K., University Press, 1983: 327-334.

13. Mindlin, R.D. An Introduction to the Mathematical Theory of Vibration of Elastic Plates. Fort Monmouth, NY, US Army Signal Corps Engineering Laboratories, 1955.
14. Bertoni, H.L. and Tamir, T. Unified theory of Rayleigh-angle phenomena for acoustic beams at liquid-solid interfaces. Applied Physics 2, 1973: 157-172.
15. Barbagelata, A., Michelozzi, E., Rauch, D., & Schmalfeldt, B. Seismic sensing of extremely-low-frequency sounds in coastal waters. In: ICASSP 82, Proceedings of the IEEE International Conference on Acoustics, Speech and Signal Processing, Paris, France, 3-5 May 1982. Piscataway, NJ, IEEE Service Center, 1982: pp 1878-1881.

KEYWORDS

ACOUSTIC RADIATION
ACOUSTICS
ADIABATIC APPROXIMATION
ANTI-SYMMETRIC
ASSYMETRIC RADIATION
ATTENUATION
BACK-SCATTERING
BASALT
BATHYMETRY
BEAM DISPLACEMENT
BEAM DIVERGENCE
BEAM REFLECTION
BEAM SPLITTING
BEAMWIDTH
BESSEL FUNCTION
BOTTOM BOUNCE
BOTTOM INTERACTION
BOTTOM-LOSS
BOTTOM
BOUNDARY CONDITIONS
BT THEORY
CHEMICAL RELAXATION
COMPLEX REFLECTION COEFFICIENT
COMPRESSIONAL WAVE
CONICAL WAVE
CONTINENTAL SHELF
CONTINUOUS BEAM
CONTINUOUS SPECTRUM
CONVERGENCE ZONE
CRITICAL ANGLE
CYLINDRICAL DISPLACEMENT
CYLINDRICAL SPREADING
DAMPING
DEEP SOUND CHANNEL
DEEP WATER
DENSITY DISCONTINUITY
DIFFRACTION
DISCRETE SPECTRUM
DISPERSION
DIVERGING BEAM
DOWN-SLOPE
DUCT RADIATION
DUCTED PROPAGATION
DUCTS
EIGENVALUE EQUATION
ELASTIC MEDIUM
ENVIRONMENT
EXCITATION
FAST FIELD PROGRAM
FAST FOURIER TRANSFORM
FINITE ELEMENT
FLAT BOTTOM
FLUID/SOLID INTERFACE
FOCUSED BEAM
FREE SHEAR VIBRATION
FREE SPACE
FREE-SURFACE
FREQUENCY
GAUSSIAN ELIMINATION
GEOMETRICAL SPREADING
GOOS-HAENCHEN EFFECT
GRAZING ANGLE
GREEN'S FUNCTION
HANKEL FUNCTION
HIGH INTENSITY
HIGH-FREQUENCY
HOMOGENEOUS SOLID LAYERS
HOOKE'S LAW
HORIZONTAL WAVENUMBER
HORIZONTALLY STRATIFIED OCEAN
HYPERGEOMETRIC FUNCTIONS
INDEX OF REFRACTION
INTEGRATION
INTERFACE MODE
INTERFACE
INTERFERENCE NULL
ISOLOSS CONTOUR
ISOTROPIC ELASTIC CONTINUA
ISOVELOCITY
KRONECKER DELTA SYMBOL
KUTSCHALE TECHNIQUE
LAME CONSTANT
LATERAL WAVE
LAYERED MEDIA
LAYERING
LEAKY SURFACE WAVE
LIMESTONE
LINEAR VISCOELASTIC
LOSSY BOTTOM
LOW FREQUENCY
LOW INTENSITY
MARCHING-IN-RANGE SOLUTION
MODE CONVERSION
MODE COUPLING
MODE CUT-OFF
MODE
MODELS
MULTILAYERED
NARROW ANGLE APPROXIMATION
NARROW BEAM
NATURAL VIBRATIONS
NEARFIELD EFFECTS
NUMERICAL MODELS
OCEAN
PARABOLIC WAVE EQUATION
PARALLEL BEAM
PARAXIAL APPROXIMATION
PARTICLE DISPLACEMENT
PARTICLE VELOCITY
PLANE WAVE
PRESSURE RELEASE SURFACE
PROPAGATION LOSS
PULSE PROPAGATION
PULSED BEAM
PULSED ULTRASONIC BEAMS

RANGE INDEPENDENT
RANGE-DEPENDENT ENVIRONMENT
RAY
RAYLEIGH ANGLE
RECURRENCE RELATIONS
REFLECTION
ROCK
ROUGH SEA BOTTOM
ROUGH SEA FLOOR
ROUGH SURFACE
SAFARI
SCATTERING
SCALAR POTENTIALS
SEA FLOOR
SEA SURFACE
SEDIMENT
SEISMIC INTERFACE WAVES
SEISMIC PULSE PROPAGATION
SHALLOW WATER
SHEAR PROPERTIES
SHEAR WAVE VELOCITY
SHEAR WAVE
SILT
SOLID LAYERS
SONAR
SOUND PRESSURE FIELD
SOUND PROPAGATION
SOUND SPEED
SPECULAR REFLECTION
SPLIT STEP MARCHING SOLUTION
SUB-BOTTOM
SURFACE WAVE
SURFACE-DUCT
SYMMETRIC BEAM
TANGENTIAL STRESS
TAPERED WAVEGUIDE
THICKNESS SHEAR FREQUENCY
THOMSON-HASKELL MATRIX METHOD
TRANSITION ZONES
TRANSMISSION LOSS
UNDERWATER ACOUSTICS
UP-SLOPE
UPWARD REFRACTION
VELOCITY POTENTIAL
VISCOSITY
VOLUME ABSORPTION
VOLUME ATTENUATION
WATER DEPTH
WATER/ALUMINIUM-OXIDE INTERFACE
WATER/STEEL INTERFACE
WAVE EQUATION
WAVE PROPAGATION
WAVENUMBER
WEDGE PROPAGATION

FREQUENCIES
500 Hz
20 Hz
2 MHz
50 Hz
25 Hz
1.5 Hz
1 Hz

INITIAL DISTRIBUTION

MINISTRIES OF DEFENCE	Copies
JSPHQ Belgium	2
DND Canada	10
CHOD Denmark	8
MOD France	8
MOD Germany	15
MOD Greece	11
MOD Italy	10
MOD Netherlands	12
CHOD Norway	10
MOD Portugal	2
MOD Spain	2
MOD Turkey	5
MOD U.K.	20
SECDEF U.S.	68

NATO AUTHORITIES	Copies
Defence Planning Committee	3
NAMILCOM	2
SACLANT	10
SACLANTREPEUR	1
CINCWESTLANT/COMOCEANLANT	1
COMSTRIKFLTANT	1
COMIBERLANT	1
CINCEASTLANT	1
COMSUBACLANT	1
COMMAIREASTLANT	1
SACEUR	2
CINCNORTH	1
CINCSOUTH	1
COMNAVSOUTH	1
COMSTRIKFORSOUTH	1
COMEDCENT	1
COMMARAIRMED	1
CINCHAN	3

SCNR FOR SACLANTCEN	Copies
SCNR Belgium	1
SCNR Canada	1
SCNR Denmark	1
SCNR Germany	1
SCNR Greece	1
SCNR Italy	1
SCNR Netherlands	1
SCNR Norway	1
SCNR Portugal	1
SCNR Turkey	1
SCNR U.K.	1
SCNR U.S.	2
SECGEN Rep. SCNR	1
NAMILCOM Rep. SCNR	1

NATIONAL LIAISON OFFICERS	
NLO Canada	1
NLO Denmark	1
NLO Germany	1
NLO Italy	1
NLO U.K.	1
NLO U.S.	1

NLR TO SACLANT	
NLR Belgium	1
NLR Canada	1
NLR Denmark	1
NLR Germany	1
NLR Greece	1
NLR Italy	1
NLR Netherlands	1
NLR Norway	1
NLR Portugal	1
NLR Turkey	1
NLR UK	1
NLR US	1

Total initial distribution	249
SACLANTCEN Library	10
Stock	21
Total number of copies	280